Canadian Science Publishing | **Canadian Geotechnical Journal**

Large deformation analysis of intermittent pile penetration into dense sand incorporating a state dependent Mohr–Coulomb model

Journal:	*Canadian Geotechnical Journal*
Manuscript ID	cgj-2023-0090.R1
Manuscript Type:	Research Article
Date Submitted by the Author:	n/a
Complete List of Authors:	Ye, Rongrong; Zhejiang University Huang, Zhongyuan; Zhejiang University Yang, Zhongxuan; Zhejiang University, Department of Civil Engineering Guo, Ning; Zhejiang University, Civil Engineering Jardine, Richard; Imperial College London, Department of Civil Engineering
Is the manuscript for consideration in a Special Issue or Collection?:	Not applicable (regular submission)
Keyword:	driven piles, large-deformation analysis, cyclic installation process, stress field, sand

Large deformation analysis of intermittent pile penetration into dense sand incorporating a state dependent Mohr–Coulomb model

R. R. Ye, Z. Y. Huang, Z. X. Yang, N. Guo, R. J. Jardine, and S. Fu

Author 1: R. R. Ye, BEng.
Graduate student, Department of Civil Engineering, Zhejiang University, Zhejiang, P. R. China
Email: 12012033@zju.edu.cn
Author 2: Z. Y. Huang, MEng.
Former graduate student, Department of Civil Engineering, Zhejiang University, Zhejiang, P. R. China
Email: 21912014@zju.edu.cn
Author 3: Z. X. Yang, Ph.D.
Professor, Department of Civil Engineering, Zhejiang University, Zhejiang, P. R. China (Orcid:0000-0003-4632-1355).
Author 4: N. Guo, Ph.D.
Assistant Professor, Department of Civil Engineering, Zhejiang University, Zhejiang, P. R. China (Orcid: 0000-0002-5515-9911)
Email: nguo@zju.edu.cn
Author 5: R. J. Jardine, Ph.D.
Professor, Department of Civil and Environmental Engineering, Imperial College London, SW7 2AZ, UK.
Email: r.jardine@imperial.ac.uk
Author 5: S. Fu, Ph.D.
Power China Huadong Engineering Corporation Limited, former Graduate student of Zhejiang University, Hangzhou 311122, China.
Email: fu_s@hdec.com

Corresponding author: Z. X. Yang (zxyang@zju.edu.cn)

Abstract

The challenges of predicting the stresses acting around piles driven in sand limits meaningful analysis of their single and group loading responses, aging processes and scale/in-situ stress level dependency. Benchmark local stresses measurements made in the sand mass and pile shaft in Calibration Chamber (CC) models show that sharply different regimes act when the pile is either penetrating or temporarily stationary. This paper presents an Arbitrary Lagrangian–Eulerian (ALE) finite element simulation of installation into dense sand, highlighting the stress changes developed between intermittent penetration stages and exploring the effects of initial stress level. The installation by cyclic jacking of closed-ended model piles studied in a highly-instrumented CC experiments is simulated with a state-dependent Mohr–Coulomb model calibrated to high-quality element tests on the sand employed. The predicted pile head loads and local stresses are compared with the CC experiments, showing generally good agreement over the lower parts of the pile shaft while also matching key field-scale trends from CPT-based practical design approaches. More advanced constitutive modeling appears necessary to eliminate discrepancies noted over the higher shaft levels, which may be linked to currently neglected aspects of the sands' highly non-linear behavior, including grain crushing and hysteresis under cyclic loading.

Keywords: driven piles, sand, large-deformation analysis, cyclic installation process, calibration chamber test, stress field

1. Introduction

Large numbers of piles are driven routinely to support onshore and offshore structures located at sand sites, including many offshore wind turbines. Research based on field testing with instrumented piles has led to more reliable methods for estimating driven pile axial capacity in sands by recognizing the close correlation of local shaft and base resistances with CPT tip resistance q_c and the normalized relative pile tip depth h/R (Lehane et al 1993, Chow 1997) and incorporating these into practical design methods (for example Jardine et al 2005, Lehane et al 2005, Lehane et al 2020). These new approaches reduce considerably the scatter and bias implicit in earlier methods of axial capacity prediction for piles driven in sand (Yang et al 2015a, b, 2017). However, the most widely employed alternative CPT based approaches employ different approaches to account for the potential effects of in-situ (free field) vertical effective stresses that lead to significant differences when applied to large offshore piles (Scarfone et al 2023). Another important feature observed in the field that has prompted much recent research is the marked effect on axial capacity in sands of age after driving (see for example Chow 1997, Axelsson 2000, Jardine et al 2006, Rimoy et al 2015, Cathie et al 2023, and Jardine 2023).

Numerical modelling provides an alternative tool for investigating pile installation and loading behavior in sand. While the finite element method (FEM) offers a well-established geotechnical analysis approach, severe element distortions occur in standard Lagrangian FEM analyses of large deformation problems such as pile penetration. Coupled Eulerian–Lagrangian (CEL) and arbitrary Lagrangian–Eulerian (ALE) FEM methods have been developed to tackle these problems. In CEL, the pile can be treated as a rigid Lagrangian body, whereas the soil is modeled as a Eulerian body that can flow inside a spatially fixed mesh to avoid element distortions (Qiu et al 2011, Ko et al 2016). In ALE, a re-meshing procedure is applied throughout the calculation process to accommodate the large deformation of soil (Zhang et al 2013, 2014, Jardine and Yang 2018, Yang et al 2020, Fu et al 2023). Other potential numerical procedures include the discrete element method (DEM) (Butlanska et al 2014, Wang and Zhao 2014, Liu and Wang 2016, Ciantia et al 2020), the material point method (MPM) (Tehrani et al 2016, Phuong et al 2016, Lorenzo et al 2018) and the particle finite element method (PFEM) (Monforte et al 2019, Hauser and Schweiger 2021, Zhang et al 2021).

Such numerical analyses of displacement pile installation have mostly concentrated on steady, monotonic, displacement-controlled penetration without modelling the individual driving/jacking cycles or the grain crushing that accompanies the installation of real piles; see Yang et al (2010). One exception is the three dimensional DEM analyses by Ciantia et al (2020) which involved crushable granular particles and considered cyclic jacking by slowly displacing the pile head upwards until the axial force reduced to zero during pause periods. Their results showed encouraging agreement with the CC experiments reported by Jardine et al (2013a, b).

Recent numerical studies including FEM-ALE (Yang et al. 2020, Fu et al. 2023), MPM (Gao et al. 2022, Fu et al. 2024), and DEM (Guo et al. 2024) analyses, have successfully reproduced most features of the model tests. However, the studies continue to reveal some limitations, such as overpredicting the radial effective stress σ'_{rc}, failing to capture the interface dilation $\Delta\sigma'_{rd}$ (increase in radial effective stress), underestimating the h/R effect, and not considering either the cyclic effects of pile installation or the impact of varying in-situ 'free-field' vertical effective stress level σ'_{v0}.

This study aims to evaluate the impact of (i) stop/start of jacking strokes during the pile installation process on the pile-soil interaction and (ii) the initial σ'_{v0} level. A non-hysteretic constitutive model is used, allowing both stationary and moving stresses to be distinguished in the analysis, although a hysteretic model could provide more accurate results. The analyses also investigated the effects of σ'_{v0} on σ'_{rc} and q_c profiles for closed-ended piles through parametric studies considering effective overburden pressures ranging from 50 to 550 kPa. Examining this question through numerical studies was far less challenging than conducting expensive and time-consuming high-pressure experiments.

This paper presents an Arbitrary Lagrangian–Eulerian (ALE) finite element numerical simulation of intermittent pile penetration, which represents the jacking and driving strokes in practice. The simulation, conducted on dense sand, identifies the stress changes developed during and between each incremental stage of penetration. It modelled a closed ended model pile, as employed in earlier cyclically jacked CC experiments and advanced the ABAQUS ALE approach described by Yang et al (2020) to include multiple push and pause phases through a hybrid displacement–load control method. A state-dependent Mohr–Coulomb model was calibrated against high-quality laboratory tests and applied to capture the sand's state-dependent behavior. Its predictions for the stationary and moving stresses invoked by pile installation are quantitatively compared with the experimental observations documented by Jardine et al (2013a, b) and earlier monotonic steady penetration simulations by Yang et al (2020) to help identify any further physical features that need to addressed to allow fully representative analyses to be made of driven pile installation in sands.

2. Calibration Chamber (CC) Experiments

Joint research by Imperial College London (ICL) and Institut Polytechnique de Grenoble (INPG) addressed the impact of pile installation on the sand and pile stress regimes through highly instrumented tests that allowed the local radial (σ_r), circumferential (σ_θ), and vertical stresses (σ_z) to be measured during the installation and load testing of a closed ended displacement pile, achieving observations that could not be made in the field (Jardine 2013, Jardine and Yang 2018). Their well-configured CC comprised three metal rings, each with 1.2 m inner diameter and 0.5 m height bolted together to form a 1.5 m deep chamber and their mini-ICP stainless-steel model pile had a radius (R) of 18 mm. Its shaft was air-abraded to an average centerline surface roughness of ~4 µm, and its tip was equipped with a 60° cone to be comparable with pilot CPT tests. The pile shaft was instrumented with 3 clusters of sensors at three depths, h, above the pile tip (h = 6.7R, 21.7R, and 41.7R) and oriented at 3 radial directions with an interval of 120°, including the axial load cells to measure the average shaft friction, and special surface stress transducers to measure the local radial and circumferential stresses on the pile shaft.

Fine silica NE34 Fontainebleau sand was air-pluviated into the chamber with an average initial void ratio e_0 = 0.62 (relative density D_r = 72%). A surcharge pressure of

150 kPa was applied on the top surface to match the stress state in field tests reported by Jardine et al (2006). Pluviation was halted at three stages to allow dozens of strain-gauged soil stress cells to be deployed in the sand at radial distances between 2*R* and 20*R* from the pile axis to measure cylindrical normal stresses σ_r, σ_ϑ and σ_z taking careful account of the very considerable cell action shown by such cells in sands; see Zhu et al (2009). Yang et al (2010), Jardine et al (2013a, b) and Rimoy et al (2015) describe several experimental studies with these arrangements. The study of the stresses developed around the mini-ICP reported by Jardine et al (2013a, b) in experiments that employed jack strokes of 5 and 10 mm length, with full relaxation of pile head loads between each stroke, provide a benchmark against which numerical analyses of pile installation using FEM (Zhang et al 2013, 2014, Yang et al 2020), DEM (Wang and Zhao 2014, Liu and Wang 2016, Ciantia et al 2020) and MPM (Lorenzo et al 2018, Gao et al 2022) have been tested.

3. Numerical Modeling

3.1. Numerical model

The code ABAQUS employed for the present study offers both CEL and ALE options for large displacement analyses. As the CEL treatment could not model the surcharge pressure applied over the sand mass in the CC tests (Yang et al 2020), two-dimensional (2D) axisymmetric ALE analyses were undertaken to simulate the intermittent pile installation process. The 18 mm radius mini-ICP was treated as a rigid Lagrangian body with a total length of 1.5 m. The final embedment length into sand (L) was 1 m ($L/R \approx$ 56). As shown in Fig. 1, to match the boundary conditions, the true CC dimensions were employed i.e., the radial width w = 0.6 m (w/R = 33.3) and height H = 1.5 m. The nodes on the two lateral boundaries were constrained to only move in the vertical direction.

The pile–sand interface behavior was governed by a surface-to-surface frictional contact algorithm, which includes formulations to model both sticking and finitesliding contacts between the two bodies. The rigid pile and deformable sand were treated as master and slave surfaces, respectively. The penalty friction formulation was applied with a friction coefficient of 0.49 (≈ tan26°), taking from the interface friction angle of 25°-27° measured from the interface ring shear tests conducted by Yang et al (2010). Default ALE adaptive remeshing was applied for the whole domain throughout the simulation, and the ABACUS remeshing frequency parameter was set to 10 while the intensity parameter was taken as 1. This indicated that the mesh was re-meshed every 10 adaptive numerical increment steps, while for each remeshing increment (a time increment based on convergence), one mesh sweep iteratively over the adaptive mesh domain was employed to relocate nodes and create a smoother mesh, according to ABAQUS (Dassault Systèmes Simulia 2016). The mesh density and pile penetration rate were selected on the basis of the careful convergence studies of Yang et al (2020). A penetration velocity of 0.05 m/s was adopted.

3.2. State-dependent Mohr–Coulomb model

The dry NE34 Fontainebleau sand employed for testing was regarded as deformable soil with a unit weight $\gamma = 16$ kN/m^3 and a Poisson's ratio $v = 0.3$, after Dano et al (2004). As shown by Verdugo and Ishihara (1996) and Altuhafi et al (2018), the mechanical behavior of sands is significantly influenced by their shear strain levels and states, as characterized at any point by their mean normal stress and void ratio. Considering the large variations of strain and stress levels and void ratios applying across the domain during the pile installation process, it was vital that the constitutive model selected to model the sand should reflect its state dependent properties.

Recent studies (Yang et al 2020 and Fu et al 2023) have found that a modified Mohr–Coulomb model can give satisfactory simulations of monotonic displacement pile installation, provided the key parameters are made state-dependent and are calibrated carefully against high-quality element tests conducted over appropriate pressure ranges. The tests show how dilatancy and friction angles, ψ and φ respectively, should be varied to match the mean effective stresses, plastic shear strains and void ratios developed at different locations in the sand mass and adjusted iteratively at different installation stages. Fu et al (2023) had to adopt a non-linear, pressure dependent, treatment for the sand's pre-yield behavior to model the strain fields observed through Digital Image Correlation observations made in other calibration chamber tests conducted at Purdue University. To avoid convergence problems, a simpler constant linear-elastic stiffness was assumed for each case considered in this study. However, this simplification did not recognize that local sand stiffnesses reduce sharply (at given effective stress levels) as strain levels grow during pile penetration, while marked mean effective pressure increases have the opposite effect. The linear elastic approach adopted also fails to capture the marked impact of stress or strain reversals on the sand's non-linear stiffness relationships.

In all other aspects the state-dependent Mohr–Coulomb yielding model employed in this study is compatible with critical state theory, which asserts that the soil reaches the critical state when it deforms under extended shearing with constant stress and volume.

The critical state void ratio e_c is a function of the mean effective pressure p', and can be expressed as (Li and Wang 1998):

$$e_c = e_\Gamma - \lambda_c \left(\frac{p'}{p_a}\right)^\zeta \quad (1)$$

where e_Γ, λ_c and ζ are three material constants obtained from conventional triaxial tests, and p_a = 101 kPa is the atmospheric pressure. The state parameter ξ described by Been and Jefferies (1985) is used to capture the variations of both friction and dilation angle with current sand conditions:

$$\xi = e - e_c \quad (2)$$

where e is the current void ratio, and e_c is the critical state void ratio at the current mean pressure p' calculated using Eq. (1). The dilatancy D is related to the state parameter using the following expression proposed by Li and Dafalias (2000):

$$D = d_0 \left[\exp(m\xi) - \frac{\eta}{M} \right] \quad (3)$$

where d_0 and m are two model parameters, η is the stress ratio and M is the critical state stress ratio. According to Mohr–Coulomb model, failure occurs if $\eta = M$ and thus the dilatancy can be obtained as

$$D = d_0[\exp(m\xi) - 1] \approx d_0 m\xi = n_\mathrm{d}\xi \tag{4}$$

where n_d is a parameter combining d_0 and m. The dilatancy angle is expressed as a function of the state parameter:

$$\psi = \arctan(-D) = \arctan(-n_\mathrm{d}\xi) \tag{5}$$

Classical Mohr–Coulomb soil models cannot simulate the drained strain-softening behavior of dense sands. To overcome this, the state parameter is introduced into the angle of shear resistance:

$$\varphi = \arctan[\tan(\varphi_\mathrm{c})\exp(-n_\mathrm{b}\xi)] \tag{6}$$

where φ_c is the critical state angle of shear resistance, and n_b is a parameter associated with φ. Further details are given by Gao et al (2022).

Based on drained triaxial tests on fresh Fontainebleau NE34 sand reported by Dano et al (2004), Gaudin et al (2005), Andria-Ntoanina et al (2010), Altuhafi and Jardine (2011), Aghakouchak (2015) and Altuhafi et al (2018), a relationship was fitted between the state parameter ξ and dilatancy angle ψ and shear resistance angle φ as shown in Fig. 2. The state-dependent Mohr–Coulomb model parameters are summarized in Table 1.

To demonstrate the performance of the model and the validity of the calibrated parameters, experimental data of drained triaxial compression tests on Fontainebleau sand reported by Andria-Ntoanina et al (2010) are simulated and compared, with the test conditions listed in Table 2.

As shown in Fig. 3(a), the simulations broadly match the test results, including the dense sand's strain-softening response. Nevertheless, apparent discrepancies can be observed between the model responses and the test data. For example, the pressure-independent linear elastic stiffness treatment fails to capture the different initial slopes in the q–ε_a curves for different p'_0 conditions. The model also overestimates the dilation seen in Fig. 3(b).

The present study aimed to extend the monotonic penetration analyses by addressing the multiple loading–unloading cycles imposed in the jacked pile CC experiments or the driving cycles implicit in driving piles in the field.

The outcomes from the present study can then identify the need, or otherwise, for still more challenging analyses to be developed involving more advanced constitutive models that could simulate the sand's non-linear behavior more representatively under monotonic and cyclic loading.

3.3. Implementation of the cyclic installation process

Field installation of driven or jacked piles usually involves advancing their tips to design depth incrementally through multiple load-unload jacking or driving cycles. Each penetration cycle applied in the CC tests, involved advancing the mini-ICP into the dense sand by a specified displacement and at a controlled rate during which the maximum moving stresses were recorded, followed by a brief pause and then an unloading stage in which the pile head load as released, after which the stationary stresses were recorded before the next penetration cycle was applied. The shaft resistances fell sharply and switch to become negative after unloading to counteract the 'locked-in' residual base load. All such load–unload cycles involve two-way shaft failure.

Before each simulation commenced, gravity and top surcharge pressures of 150 kPa were applied, treating the sand mass as being purely elastic, leading to an average initial state parameter of -0.16 for the sand mass prior to pile installation. To simulate the pile installation process, including both the push and pause stages, a hybrid cyclic displacement–load control method was adopted. The same number of cycles as the CC test is considered, each consisting of a push stage performed by displacing the pile steadily to the given penetration increment. After a short pause, the head load was fully released before imposing a second short pause and then such cycles were repeated until the full penetration is achieved. To simulate the unloading stages, a point mass was assigned to the head of the pile, which is referred to as the reference point (RP). The point mass is equal to the lumped mass of the pile, and the RP has three translational degrees of freedom (DoF). At the beginning of the final pause stage, only the vertical DoF is released, and the head load is maintained at zero as the RP rebounds vertically, as in the experiments. The present study assessed the impact of advancing the pile tip by increments of 5 to 20 mm per jack stroke, giving 50 to 200 jacking cycles in total for each installation. One consequence of adopting a non-hysteretic sand model was that the spatial distributions of stresses achieved at any given pile tip depth were largely insensitive to the stroke length or jacking cycle taken to reach this depth. The results given below focus mainly on the outcomes of analyses run with 50 mm strokes in which 200 cycles were applied to reach 1 m of penetration.

A further physical feature that was not captured in the numerical analysis was the marked rise seen with 36 mm diameter laboratory model and 102 mm diameter field tests in the shaft radial effective stresses through local dilation that occurs at the sand–steel interface as the shaft is loaded to failure. As captured in the ICP-05 and UWA-05 design procedures, this results from grains having to unlock from the shaft's finite roughness and impose radially outward displacements of similar magnitude to the average peak-to-trough roughness of the pile shaft, ≈4 μm for the experimental mini-ICP pile. Special interface routines would be required to capture the impact of this 'dilative' component, which increases linearly with pile roughness and sand shear stiffness but reduces inversely with pile diameter. This option was not available for the present analyses

4. Results and discussions

The predictions of greatest interest in this paper are the moving and stationary stresses developed on the pile shaft and within the sand mass, as predicted from ALE analyses and measured in the calibration chamber. In the following analysis, the subscripts 'm' and 's' denote the moving and stationary stresses, respectively.

However, consideration is given first to the ALE predictions for the pile tip resistances, which are effectively the same as CPT tip resistances as the pile tip has the same geometry as a standard CPT cone. We concentrate first on the case involving a fixed vertical overburden stress σ'_{vo} = 150 kPa, as employed in the benchmark CC experiments. The impact of varying σ'_{vo} is considered subsequently.

4.1. Cone resistance and head/base forces

The numerical q_c profile prediction is an important indicator of the capacity of the constitutive model adopted in the simulation to give representative predictions. Fig. 4 compares the numerical results for the σ'_{vo} = 150 kPa case, using the present state-dependent Mohr–Coulomb model and that by Yang et al (2020), with the experimental data. They exhibit similar profiles and stabilize to q_c approximately 19 MPa and 21 MPa respectively at $z/R \geq 20$. Remarkably, the q_c profile predicted using the state-dependent Mohr–Coulomb model exhibits smaller oscillations and more stable trends than those obtained by Yang et al (2020) in monotonic penetration analyses. The subsequent stress measures are normalized by the respective q_c values to aid comparison between the numerical, experimental results and CPT based pile design methods.

Fig. 5 illustrates the development of the predicted head and base forces and shaft frictional force of the model pile during penetration, along with the measured head forces in the experiment after the 10^{th} cycle. While the numerical head force is slightly larger than that measured, they show broad agreement. The numerical pile head force reaches 25~40 kN in the pushing stage and reduces to zero in the pause stage, while the pile base force reaches 18~20 kN during the pushing stage. Rather than reducing to zero during pause stages, significant locked-in residual loads develop. During the pushing phase, the pile shaft experiences upward frictional forces, which contribute significantly to the overall ultimate bearing capacity in conjunction with the base forces. These frictional forces reverse direction during unloading to reach equilibrium with the locked-in base forces.

4.2. Preliminary assessment of impact of jacking cycles

A preliminary assessment of the impact of the load-unload cycles is shown in Fig. 6 considering the (i) end-of-push moving and (ii) end-of-pause stationary radial stresses developed in the sand mass at r/R = 2 (36 mm from the pile axis) and z/R = 15.8 (285 mm below the ground level) for over a cycle imposed after the pile tip had penetrated to a depth Lp / R = 14.4 (260 mm below the ground level), where r is the radial distance from the pile axis, and z is the depth below the sand surface. The cyclic stress path measured in the model test is depicted in Fig. 6(a): the section from point C to point A covers a typical pushing phase in which the normalized radial stress increases monotonically as the tip penetrates and the end-of-push and maximum moving stress obtained at point A. The release of pile head load to zero leads to an upward pile rebound to point B and a considerable radial stress reduction by the end of the stationary pause period. The simulation in Fig. 6(b) shows broad agreement with the experimental counterpart, although the unloading rebound displacement is larger than measured, while the radial stress relaxation is under-predicted.

4.2. Variations in sand state developed during installation

Dramatic changes take place in the sands' state around the pile shaft and tip, which can be quantified by the state parameter ξ. Figs. 5(a), (b) and (c) exhibit contour plots of the mean normal stress, volumetric strain and (regularly updated) local state parameter variations after the pile installation, respectively. As noted earlier, ξ = -0.16, prior to pile installation due to its self-weight and the imposed surcharge pressure.

During pile penetration, extremely high mean normal stresses are predicted near the pile tip. While grain crushing, and by implication large local volume straining ε_v was observed in the CC experiments (Yang et al 2010), the linear elastic Mohr-Coulomb model employed predicts relatively small volume changes in the compression region. As shown in Fig. 7(c), a region of near zero ξ extends out to approximately 2R approximately from the region beneath the tip (0> h/R > -2) and forms an annulus surrounding the entire pile shaft, signifying that this mass of sand is shearing under nearly critical state conditions. As the pile penetrates, the sand beneath the pile tip is forced to flow downward and radially outwards. Very significant stress relaxation takes place as the pile tip passes and large dilative strains that keep the sand close to critical state conditions. The $\partial \varepsilon_v/\partial(r/R)$ gradients are much steeper than those for $\partial p'/\partial(r/R)$ above the tip in $2 < r/R < 3$ region, leading to a considerable change of sand state near the pile shaft. However, the state parameter tends to decrease gradually with r/R and falls towards the initial 'undisturbed' value of -0.16 at $r/R > 18$, as the far-field sand's states are less influenced by the installation process.

4.3. Radial stress changes

Jardine et al (2013a) describe how and why their radial CC sand mass stress measurements were inherently more reliable than their (far more challenging) circumferential and vertical stress observations. Fig. 8 illustrates the variations of moving radial stresses normalized by q_c with pile penetration depth L_p at a radial distance of $r/R = 2$ from the pile axis and three fixed depths below the sand surface. Both the simulation (Fig. 8(a)) and experiment (Fig. 8(b)) show a marked increase in radial stress as the pile tip approaches the instrument level and a peak as it passes this depth and a sharp decay as the tip continues to penetrate to greater depth. While the ALE analysis broadly captures the experimental profile, the measured moving radial stress maxima are slightly higher than those predicted at $z/R = 10.6$ and 30.6, while slightly lower than predicted stresses at $z/R = 46.1$. As explored in greater detail later, the stresses developed after the pile tip has passed each instrument level are significantly over-predicted.

The corresponding profiles of the stationary radial stresses developed when the pile is fully unloaded during jacking pauses are displayed in Fig. 8(c) and (d), while Fig. 9 further compares the numerical and experimental radial stresses at different locations, plotted as a function of relative pile tip depth h normalized by the pile radius R, where h/R is negative initially and then becomes positive when the pile tip passes each level of the stress cells. The stationary traces follow a similar pattern to the moving stresses, but with notably lower maximum stationary stresses than their moving counterparts. While the predictions generally match the experimental trends results, the stationary radial stresses expected after the pile tip has passed each instrument depth (giving $h/R > 0$) are generally significantly over-predicted, while the peak stationary radial stresses tend to be under-predicted.

Fig. 10 considers how the normalized moving radial stresses vary with normalized distance from the pile axis (r/R) for levels just above the pile tip, at $h/R = 0.5$. The numerical and experimental results indicate similar exponential decays with the increasing r/R. As shown in Fig. 10(a), σ'_{rm} reaches a peak value of $0.34q_c$ close to the pile–soil interface at $r/R \approx 0.29$. While it was not possible to measure the stresses at such positions in the experiments. Jardine et al (2013a) estimated the maximum radial stress value of $\sigma'_{rm} \approx 0.33q_c$ at the same position from the assumed triaxial compression failure conditions, taking critical state $\varphi'_{cs} = 30°$ for the sand and assuming the vertical stress $\sigma'_z = q_c$. Jardine et al (2013a) also argued that larger φ' values could be realized in the intermediate stress zone located above the tip, and laterally within $1 < r/R < 3$, where the sand has experienced high pressures, crushing and radial displacement prior to unloading as the tip passed. However, the numerical simulation could not confirm this, because such considerations were beyond the simplified sand model adopted in this study.

Jardine et al (2013a) examined how the radial stresses decay with r/R at positions near the tip. Linear logarithmic fits over the $1 < r/R < 20$ range indicated power-law exponents of -1.1 from the simulation and -1.23 from the experiment that fall in the ranges inferred from spherical expansion and cylindrical expansion analyses (Jardine et al 2013a). However, gentler gradients are seen closer to ($r/R < 1$) and further from ($r/R > 20$) the pile tip.

Further consideration is given in Fig. 11 to the stationary radial stresses developed during jacking pauses, considering four levels above the pile tip (h/R = 5.6, 20, 31.1

and 40.6) showing both predictions and experimental results. These plots confirm that the maximum radial stresses develop out within the soil mass rather than on the pile shaft, as noted previously (Zhang et al 2014, Yang et al 2020, Ciantia et al 2020). The maximum stationary radial stresses (2.8~4.4%q_c) are predicted to develop at r/R = 3~4 and be 1.5 to 2 times those expected on the pile shaft at r/R = 1. The radial stresses fall with r/R and stabilize at ≈ 0.8%q_c at r = 30R, slightly higher than the free-field radial stresses. The stationary radial stresses developed on the pile shaft show a clear trend to reduce with relative shaft tip depth h/R, which was termed the 'h/R effect' by Lehane et al (1993) and 'cyclic fatigue' by White and Lehane (2004). The predictions shown here are purely artefacts of the problem geometry and the assumed sand properties: they include no allowance for any effects of cyclic loading or 'fatigue'. These predictions show a systematic trend to over predict the stresses developed at higher h/R values. Although there are still some discrepancies due to the simplified treatment of the sand's stiffness and cyclic behavior, the model predicts the key features of how the stress distributions vary with r/R and reduce with h/R.

Radial stress contour maps covering h/R from -10 to 10 and r/R 0 to 10 are plotted for the final (moving) push-of-installation and immediately post-installation stationary cases in Fig. 12. The numerical σ'_r/q_c contours match well with the experimental data at the span of h/R = -10~2 and r/R = 2~10, while discrepancies are observed at points higher above the tip.

Predicting the stationary radial stress profiles developed over the pile shafts and knowing how they change under axial loading is central to estimating the piles' axial capacities. The Fig. 12 contour plots show that the stress cycles developed are considerably higher when the pile is moving than when stationary, as emphasized by Jardine et al (2013a, b), and are most intense in the region close to the pile tip (h/R = -2~2 and r/R = 0 or 2~5). The contours also confirm the convenience of considering the radial stresses σ'_r as: (i) being proportional to q_c and (ii) spatial functions of h/R and r/R, as is implicit in modern CPT-based pile design methods such as ICP-05 (Jardine et al 2005) and UWA-05 (Lehane et al 2005). ICP-05 stipulates that σ'_r/q_c grows in proportion to $(\sigma'_{v0}/p_a)^{0.13}$, while UWA-05 and the new Unified method (Lehane et al (2020) assume the ratios to be insensitive to σ'_{v0}.

While we investigate this question in a later section, we highlight in Fig. 13 (a) to (d) that disparities between predictions and measurements apply within the sand mass at higher h/R levels. Here, the trends with h/R for normalized moving and stationary radial stresses σ'_r/q_c are plotted considering radial positions of r/R = 2 and 3 respectively. ALE analysis predictions made applying three different stroke lengths are shown along with data from two Mini-ICP experiments that required 100 and 200 jacking cycles to achieve full penetration. The numerical results are both insensitive to the number of jacking cycles and significantly over-predict the experimentally observed radial stresses at h/R > 3. These over-predictions may be attributed to the simple linear, pressure-independent and non-hysteretic pre-yield treatment model adopted in the analysis, which cannot capture the expected tendency of the sand around the shaft to contract with each cycle of the jacking or driving pile installation process. Furthermore, the analysis neglects the significant particle crushing that occurs beneath the pile tip and the volume changes that result. Yang et al (2010) have shown experimentally how the crushed sand is displaced upward to form a thin annulus around the shaft. Further grain breakage develops within this abrading shear band, as well as creep deformations induced by the extreme tip stresses and grain breakage, all of which can be expected to reduce the radial, near shaft, stresses. In addition, the ALE analysis did not capture the constrained pile-to-sand interface dilation that is known to cause significant rises in the local shaft radial effective stress on the shafts of small diameter piles as they are loaded to failure.

Further insights are given in Fig. 13 (e) and (f) to the normalized moving and stationary radial stresses obtained on the pile shaft at $r = R$ from the ALE analysis, which are compared with measurements made at two levels ($h = 6.7R$ and $21.7R$) with the Mini-ICP's local surface stress transducers (SSTs). The radial stresses at $r = R$ are very large close to the pile tip ($h < 3R$) and decay sharply with increasing in h/R to low values, as seen in predictions and measurements for the $r = 2R$ and $3R$ locations. The experimental radial stresses measured by the Mini-ICP's SSTs in the calibration chamber tests are lower than the counterparts of the ALE results, i.e., 1.3~1.7%q_c against 2.2~3.0%q_c for moving conditions and 0.7~1.2%q_c against 2.3~2.9%q_c for stationary conditions. These plots confirm that further aspects of the sand's behavior have to be addressed in ALE analyses to capture the final reductions of shaft σ'_r values and so match the profiles developed on the shafts of model or field driven piles.

4.4. Circumferential stress

Experimental measurements of the circumferential stresses are inherently more difficult to make, especially in the near-field 1 < r/R < 3 region, than radial stresses because of the sensors' geometry in relation to the steep local stress and displacement gradients and concerns that the sensors' presence might potentially affect the near-field stresses and cause σ'_θ stress under-registration (Jardine et al 2013a). These limitations led to fewer circumferential gauges being installed. Moreover, a relatively high proportion of the circumferential stress cells placed at low r/R ratios failed as the pile tips passed by.

Normalized circumferential stresses measured at r/R = 2 are plotted against relative pile tip depth h/R in Fig. 14. Although some key measurements are missing, the general trends inferred for σ'_θ resemble the shapes of the profiles recorded for σ'_r (Jardine et al 2013a). The moving circumferential stress maxima appear to be similar at each level in both the numerical and experimental results, with an average ≈ 8%q_c, although the smaller stationary stresses appear to have been either over-predicted, or possibly under-recorded in most cases.

The $\sigma'_{\theta m}$ profiles with normalized distance from the pile axis r/R at h/R = 0.5 are presented both in linear and log–log coordinates in Fig. 15. The equivalent triaxial compression failure condition gives an estimated maximum $\sigma'_{\theta m} = \sigma'_{rm} \approx 0.33q_c$ under the centerline, while a lower 0.26q_c is predicted close to the pile–soil interface at r/R = 0.29 in the simulation. The power law decay of $\sigma'_{\theta m}$ within the range of 1< r/R < 20 has an exponent of -1.32, slightly steeper than the value for σ'_{rm}.

Fig. 16 illustrates the stationary circumferential stress measurements $\sigma'_{\theta s}$ made above the tip after the final jacking stroke. As explained above, there are very few data for $r/R < 5$, so Jardine et al (2013a) applied cylindrical stress equilibrium to interpret the near-field $\sigma'_{\theta s}$ trends from the more comprehensive and reliable radial stress dataset, as shown in Fig. 16(b). The predicted stationary circumferential stresses $\sigma'_{\theta s}$ show similar trends as the radial stresses. The $\sigma'_{\theta s}$ maxima develop at r/R = 2~3 are 4.1~6.0%q_c, with values of 1 to 2 times higher than those expected adjacent to the shaft.

Fig. 17 compares the expected and measured contour maps for normalized σ'_{θ} after the last stroke. These show σ'_{θ} ratios lower than those seen for σ'_r in Fig. 11, except for the area of locally concentrated stresses positioned around the pile shaft at r/R < 3. The numerical results significantly exceed the experimental counterparts, especially in the region where stress sensors could be placed closest to the pile (1 < r/R < 3) in the CC tests.

4.5. Vertical stress

It is even more difficult to measure vertical than circumferential stresses at points close to the pile shaft in CC tests (Jardine et al 2013a). So only the vertical stresses developed at the r/R = 3 position are considered in Fig. 18. While broadly comparable moving and stationary conditions stress maxima are indicated, the predicted stationary stress maxima are much greater than indicated by the experiments with h/R > 0, showing still more marked disparities than were seen with the corresponding radial or circumferential stress trends.

The non-dimensional moving vertical stresses developed at h/R = 0.5 shown in Fig. 19 indicate an extraordinarily steep decay with r/R in comparison with the other two cylindrical normal stresses. A maximum value of σ'_{zm} = 0.62q_c is predicted at the pile–

soil interface, which is lower than the qc assumed by Jardine et al (2013a). The moving vertical stresses decay to σ'_{zm} = 0.08q_c at r/R = 2 and stabilize at 0.01q_c beyond r/R = 10, slightly above the imposed initial stress. The power law fit gives the vertical stress decaying according to $(r/R)^{-1.56}$ within the range of 1< r/R <10.

The moving and stationary vertical stress contour maps shown in Fig. 20(a) and c) respectively give a far clearer indication of the intense stress concentrations that emanate from the pile tip maxima (shown at h/R = 0.5) than the measurements which could only be made at $r/R \geq 2$, as contoured in Fig. 20(b) and (d). Also clear is the near halving of stresses that occurs when the pile head load is released.

4.6. The influence of the free field vertical effective stress

Five further full analyses were undertaken to investigate the potential influence of σ'_{v0} on the σ'_r/q_c ratios developed at given h/R and r/R positions. Maintaining consistent geometry, initial sand void ratio and other pertinent physical parameters, the ALE numerical simulations considered CC sand mass surface surcharge pressures ranging from 50 to 550 kPa and gave a total of six cases to inspect.

Richart and Woods (1970) proposed the following nonlinear stiffness function:

$$G = G_0 \frac{(2.97-e)^2}{1+e} p_a \left(\frac{p}{p_a}\right)^{0.5} \quad (7)$$

Assuming a constant Poisson's ratio and a fixed void ratio, Eq. (7) yields:

$$E = E_a \left(\frac{p}{p_a}\right)^{0.5} \quad (8)$$

where E_a = $E(e)$ is the Young's modulus as a function of void ratio e under the atmospheric pressure p_a.

Although the constitutive model employed in this study assumed a constant Young's modulus for each calibration chamber overburden stress (σ_{v0}) case, the values were varied between the six σ_{v0} cases as shown in Table 3, taking due account of the initial void ratios reducing slightly with increasing σ_{v0}. Six further analyses were run for comparison while maintaining a single fixed stiffness E_{fixed} = 60 MPa.

Fig. 21 shows how the cone resistance q_c profile predictions obtained from the fixed and variable Young's moduli analyses varied with σ_{v0}. The results may be compared with the empirical relationships proposed by Boulanger (2003) between q_c and σ_{v0}.:

$$\begin{cases} \dfrac{q_c}{p_a} = C_0 C_1 (\dfrac{\sigma_{v0}}{p_a})^m (\dfrac{K_0}{0.45})^{m-0.077} \\ m = 0.7836 - 0.5208 D_r \\ C_0 = 25.7 + 39.7 D_r + 212.3 D_r{}^2 \\ C_1 = 1 \qquad \text{for typical set} \\ C_1 = 0.64 \qquad \text{upper bound} \\ C_1 = 1.56 \qquad \text{lower bound} \end{cases} \tag{9}$$

Eq. (9) can be rewritten as:

$$q_c = q_{c1} (\frac{\sigma_{v0}}{p_a})^m \tag{10}$$

where q_{c1} is the normalized cone resistance q_c at σ_{v0}/p_a = 1. This formula degenerates into the widely used formula by Liao and Whitman (1986) at D_r = 54%:

$$q_c = q_{c1} (\frac{\sigma_{v0}}{p_a})^{0.5} \tag{11}$$

The empirical relationships are compared with the simulated 'steady' values of q_c in Fig. 22. While the fixed and variable moduli predictions fall within the upper and lower bounds indicated by the empirical formulae, the variable modulus predictions provide far better matching values of q_{c1} and exponent *m.*

The alternative predictions for the stress conditions developed on the pile shaft are explored in Fig. 23, which shows shaft radial stress predictions for the six calibration chamber 'overburden pressure' cases and compares these with estimates given by the empirical ICP-05 design method. Again, the predictions and empirical estimates fall in broadly similar ranges, and show closest agreement at the lowest *h/R* = 5.6 pile shaft position. The analyses tend to show stresses greater than the ICP estimates at higher *h/R* levels because of the unmodeled factors discussed earlier, including the sand's non-linear stiffness and grain crushing, as well as its cyclic loading and interface dilation responses. Log-log fits of σ'_{rc} and σ'_{v0} are provided in Fig. 24, showing improbably low exponents ranging from 0.033 to 0.479 for the fixed modulus model and a more credible range of 0.317 to 0.551 for the variable modulus model. Fig. 25 considers the results further by plotting the normalized radial stresses σ'_{rc}/q_c against σ'_{v0} considering four h/R positions. The variable modulus analyses suggests the σ'_{rc}/q_c ratios developed on the shafts (at r/R = 1) of closed ended piles at fixed h/R may not depend on σ'_{v0}. This is compatible with the UWA-05 and the Unified design methods: see Lehane et al. (2020). However, the q_c and σ'_{rc} predictions are highly sensitive to the adopted stiffness relationships adopted for modelling and it is possible that analyses with more refined stiffness models might indicate a slight dependency, as is incorporated into the ICP approach.

5. Discussion

The present study aimed to begin an exploration of how the multiple loading–unloading cycles imposed in jacked pile CC experiments and the field driving of piles affect the stress regime in the surrounding soil mass. The work has demonstrated that ALE analyses incorporating the simplest sand model that might potentially offer meaningful results can cope with frequent variations in very large stress and strain changes associated with pile penetration and deliver stable results at a reasonable computational expense. The results obtained show encouraging agreement with many aspects of the pile experiments and also provide a way to explore questions such as the relationships between CPT resistances and pile tip and shaft stresses, and how these may vary with vertical effective stress level.

However, the simulations remain imperfect and tended, for example, to (i) overpredict the difference between stationary and moving stresses as well as (ii) underestimate the tendency for stresses to decay with h/R at higher levels on the pile shafts. The stresses generated by installation proved highly sensitive to the sand's constitutive behavior and we speculate that addressing grain breakage, non-linear (pressure-dependent) stiffness, hysteresis and time-dependent behavior will offer further insights and allow still closer agreement between predictions laboratory model and field and experiments.

6. Summary and Conclusions

Understanding the full stress regimes generated around piles driven in sand is vital to the development of truly representative analyses of such piles' responses to monotonic and cyclic loading, their interactions when installed in groups and the impact of pile age on field behavior.

An analysis has been presented in this paper of a closed-ended pile penetrating a pressurized calibration chamber sand mass through an intermittent jacking process involving multiple jack load-unload cycles. This has been achieved through ABAQUS ALE analyses incorporating a carefully calibrated state-dependent Mohr–Coulomb soil model and a hybrid 'cyclic' displacement–load control, in which the push and pause phases imposed in the experiments were simulated to capture the moving and stationary states of stress in the sand mass, although without incorporating a realistic sand stiffness or fully hysteretic cyclic soil model. The stress regime developed in the surrounding soil mass and considerable differences between the stresses in different stages are analyzed and discussed. The numerical results are compared with the experimental results from cyclic installation calibration chamber tests and field test trends captured within the ICP-05, UWA-05 and Unified approaches. The key conclusions are:

1. The adopted hybrid cyclic displacement–load control method provides a feasible way to model numerically the stationary cylindrical normal stresses σ'_{rs}, $\sigma'_{\theta s}$ and σ'_{zs} set up by an intermittent penetration process that better matches the field installation history of most displacement piles, as well as the CC tests employed as a benchmark experimental dataset.
2. The numerical simulations show many features that match the calibration chamber observations. Broadly representative patterns were obtained for normal

stress variations with q_c, r/R and h/R, and realistically significant differences in these stresses are identified between the push and pause stages of each pile jacking cycle.

3. The stress distributions obtained from the numerical analysis can help fill in trends that could not be observed experimentally and so inform assessment of the distributions of circumferential and vertical stress components developed at points close to the pile shaft. They also allowed an examination of the potential effects of the free field vertical stress level. However, the analyses showed clear tendencies to (i) overpredict the stationary stresses at points above the tip, where $h/R > 0$.

4. The parametric analyses of surcharge pressure effects indicated that q_c has a power function relationship with σ_{v0}/p_a, consistent with the empirical findings of Boulanger (2003) and Liao and Whitman (1986). The comparison of fixed modulus model and variable modulus model illustrated that stiffness variation must be considered when evaluating the relationship between σ_{v0} and q_c.

5. The same simplified ALE analyses indicated no significant influence of σ_{v0}/p_a on the σ'_{rc}/q_c ratios developed on the pile shaft at different h/R values. This is consistent with the UWA-05 approach and the Unified method.

6. Discussion of the results provides pointers to ways in which the analyses could be improved to become still more representative. These include, (i) the use of a non-linear, pressure dependent soil stiffness model, (ii) addressing sand grain crushing and the associated large volume changes developed beneath the pile tip, (iii) implementing a hysteretic model that can capture better the transient and irrecoverable effects of cycling and (iv) considering how time dependent soil behavior and creep may affect the stresses developed during and after installation by both rapid jacking and fully dynamic pile driving.

Competing interests

The authors declare there are no competing interests.

Data Availability

Data generated or analyzed during this study are available from the corresponding author upon reasonable request.

Acknowledgement

This research was supported by Major International Joint Research Project of NSFC (52020105003) and other projects funded by NSFC (nos. 52338008 and 52078456).

References

Aghakouchak, A. 2015. Advanced laboratory studies to explore the axial cyclic behaviour of driven piles. Doctoral dissertation, Imperial College, London, UK.

Altuhafi, F., and Jardine, R. J. 2011. Effect of particle breakage and strain path reversal on the properties of sands located near to driven piles. In Proceedings of the 5th International Symposium on Deformation Characteristics of Geomaterials, Vol. 1, Seoul. 386–395.

Altuhafi, F. N., Jardine, R. J., Georgiannou, V. N., and Moinet, W. W. 2018. Effects of particle breakage and stress reversal on the behaviour of sand around displacement piles. Géotechnique, **68**(6): 546-555.

Andria-Ntoanina, J., Canou, J., and Dupla, J. C. 2010. Caractérisation mécanique du sable de Fontainebleau NE34 à l'appareil triaxial sous cisaillement monotone. Laboratoire Navier - Géotechnique (CERMES, ENPC/LCPC).

Arshad, M. I., Tehrani, F. S., Prezzi, M., and Salgado, R. 2014. Experimental study of cone penetration in silica sand using digital image correlation. Géotechnique, **64**(7): 551-569.

Axelsson, G. 2000. Long term set-up of driven piles in sand. Doctoral dissertation, Royal Institute of Technology, Stockholm, SE.

Boulanger, R.W. 2003. High Overburden Stress Effects in Liquefaction Analyses. Journal of Geotechnical and Geoenvironmental Engineering, 129(12):1071-1082.

Butlanska, J., Arroyo, M., Gens, A., and O'Sullivan, C. 2014. Multi-scale analysis of cone penetration test (CPT) in a virtual calibration chamber. Canadian Geotechnical Journal, **51**(1): 51-66.

Cathie, D., Jardine, R.J., Silvano, R., Kontoe, S., Schroeder, F.C., 2023. Axial capacity ageing trends of large diameter piles driven in sand. Soils and Foundations, **63**(6): 101401.

Chow, F. C. 1997. Investigations into displacement pile behaviour for offshore foundations. Doctoral dissertation, Imperial College, London, UK.

Ciantia, M., O'Sullivan, C., and Jardine, R. J. 2020. Pile penetration in crushable soils: Insights from micromechanical modelling. In Proceedings of the 17th European Conf on Soil Mechanics and Geotechnical Engineering (ECSMGE-2019). 298-317.

Dano, C., Hicher, P. Y., and Tailliez, S. 2004. Engineering properties of grouted sands. Journal of Geotechnical and Geoenvironmental Engineering, **130**(3): 328-338.

Dassault Systèmes Simulia. 2016. Abaqus 2016 analysis user's manual. Providence, RI: Simulia.

Foray, P., Balachowski, L., and Colliat, J. L. 1998. Bearing capacity of model piles driven into dense over-consolidated sands. Canadian Geotechnical Journal, **35**(2): 374-385.

Fu, S., Yang, Z.X., Jardine, R.J., and Guo, N. 2023. Large deformation finite element simulation of deformation and strain fields resulting from closed-end displacement pile installation in sand. Journal of Geotechnical and Geoenvironmental Engineering, in press.

Gao, L., Guo, N., Yang, Z.X., and Jardine, R.J. 2022. MPM modeling of pile installation in sand: Contact improvement and quantitative analysis. Computers and Geotechnics, **151**: 104943.

Gaudin, C., Schnaid, F., and Garnier, J. 2005. Sand characterization by combined centrifuge and laboratory tests. International Journal of Physical Modelling in Geotechnics, **5**(1): 42-56.

Gavin, K. G., and Lehane, B. M. 2003. The shaft capacity of pipe piles in sand. Canadian Geotechnical Journal, **40**(1): 36-45.

Hauser, L., and Schweiger, H. F. 2021. Numerical study on undrained cone penetration in structured soil using G-PFEM. Computers and Geotechnics., **133**(2021): 104061.

Huang, A. B., and Hsu, H. H. 2005. Cone penetration tests under simulated field conditions. Géotechnique, **55**(5): 345-354.

Jardine, R. J. 2013. Advanced laboratory testing in research and practice: the 2nd Bishop Lecture. in Proceedings of International Conference on Soil Mechanics and Geotechnical Engineering (ICSMGE), Vol. 1, Paris, pp. 35-55.

Jardine, R.J. 2023. Time-dependent vertical bearing behaviour of shallow foundations and driven piles. 6th ISSMGE McClelland Lecture. Proc. 9th Int. Conf. on Offshore Site Investigations and Geotechnics, SUT, London, pp. 27-81.

Jardine, R. J., Chow, F. C., Overy, R., and Standing, J. R. 2005. ICP design methods for driven piles in sands and clays, Thomas Telford, London.

Jardine, R. J., Standing, J. R., and Chow, F. C. 2006. Some observations of the effects of time on the capacity of piles driven in sand. Géotechnique, **56**(4): 227-244.

Jardine, R. J., and Yang, Z. X. 2018. Joint research into the behaviour of driven piles. W. Wu and H.-S. Yu (Eds.): Proceedings of China-Europe Conference on Geotechnical Engineering, SSGG, pp. 961-972.

Jardine, R. J., Zhu, B. T., Foray, P., and Yang, Z. X. 2013a. Interpretation of stress measurements made around closed-ended displacement piles in sand. Géotechnique, **63**(8): 613-627.

Jardine, R. J., Zhu, B. T., Foray, P., and Yang, Z. X. 2013b. Measurement of stresses around closed-ended displacement piles in sand. Géotechnique, **63**(1): 1-17.

Ko, J., Jeong, S., and Lee, J. K. 2016. Large deformation FE analysis of driven steel pipe piles with soil plugging. Computers and Geotechnics., **71**(2016): 82-97.

Lehane, B. M., Jardine, R. J., Bond, A. J., and Frank, R. 1993. Mechanisms of shaft friction in sand from instrumented pile tests. Journal of Geotechnical Engineering, **119**(1): 19-35.

Lehane, B. M., Liu, Z.Q., Bittar, E.J., et al. 2020. A new ‘unified’ CPT-based axial pile capacity design method for driven piles in sand. 4th International Symposium on Frontiers in Offshore Geotechnics, Austin Texas. 462-478.

Lehane, B. M., Schneider, J. A., and Xu, X. 2005. The UWA-05 method for prediction of axial capacity of driven piles in sand. in Proceedings of the 1st International Symposium on Frontiers in Offshore Geotechnics. Perth, Australia, 683-689.

Liao, S. C., and Whitman, R. V. 1986. Overburden correction factor for SPT in sand. Journal of Geotechnical Engineering, 112(3): 373–377.

Liu, S., and Wang, J. 2016. Depth-independent cone penetration mechanism by a discrete element method (DEM)-based stress normalization approach. Canadian Geotechnical Journal, **53**(5): 871-883.

Lorenzo, R., da Cunha, R. P., Neto, M. P. C., and Nairn, J. A. 2018. Numerical simulation of installation of jacked piles in sand using material point method. Canadian Geotechnical Journal, **55**(1): 131-146.

Monforte, L., Arroyo, M., Gens, A., and Carbonell, J. M. 2019. Enhanced cone penetration test interpretation with the Particle Finite Element method (PFEM). In Proceedings of the 17th European Conference on Soil Mechanics and Geotechnical Engineering (ECSMGE-2019), 1-8.

Paik, K., and Salgado, R. 2003. Determination of bearing capacity of open-ended piles in sand. Journal of Geotechnical and Geoenvironmental Engineering, **129**(1): 46-57.

Phuong, N. T. V., van Tol, A. F., Elkadi, A. S. K., and Rohe, A. 2016. Numerical investigation of pile installation effects in sand using material point method. Computers and Geotechnics, **73**(2016): 58-71.

Qiu, G., Henke, S., and Grabe, J. 2011. Application of a Coupled Eulerian–Lagrangian approach on geomechanical problems involving large deformations. Computers and Geotechnics, **38**(1): 30-39.

Richart, F. E., Jr., Hall, J. R., and Woods, R. D. 1970. Vibration of soils and foundations. International series in theoretical and applied mechanics, Prentice-Hall, Englewood Cliffs, N.J.

Rimoy, S., Silva, M., Jardine, R. J., Yang, Z. X., Zhu, B. T., and Tsuha, C. H. C. 2015. Field and model investigations into the influence of age on axial capacity of displacement piles in silica sands. Géotechnique, **65**(7): 576-589.

Rimoy S, Silva, M. and Jardine R.J. 2022. Stability and load-displacement behaviour of axially cyclic loaded displacement piles in sands. Canadian Geotechnical Journal, in press.

Salgado, R., Mitchell, J. K., and Jamiolkowski, M. 1998. Calibration chamber size effects on penetration resistance in sand. Journal of Geotechnical and Geoenvironmental Engineering, **124**(9): 878-888.

Scarfone, R., Schroeder, F.C., Silvano, R., Cathie, D., and Jardine, R.J. 2023. Divergence between CPT based method predictions for the axial capacities of large offshore piles driven in sand. Proc. 9th Int. Conf. on Offshore Site Investigations and Geotechnics, SUT, London., pp. 986-993.

Tehrani, F. S., Nguyen, P., Brinkgreve, R. B. J., and van Tol, A. F. 2016. Comparison of press-replace method and material point method for analysis of jacked piles. Computers and Geotechnics, **78**(2016): 38-53.

Verdugo, R., and Ishihara, K. 1996. The steady state of sandy soils. Soils and Foundations, **36**(2): 81-91.

Wang, J., and Zhao, B. 2014. Discrete-continuum analysis of monotonic pile penetration in crushable sands. Canadian Geotechnical Journal, **51**(10): 1095-1110.

White, D. J., and Bolton, M. D. 2004. Displacement and strain paths during plane-strain model pile installation in sand. Géotechnique, **54**(6): 375-397.

White, D. J., and Lehane, B. M. 2004. Friction fatigue on displacement piles in sand. Géotechnique, **54**(10): 645-658.

Yang, Z. X., Jardine, R. J., Zhu, B. T., Foray, P., and Tsuha, C. H. C. 2010. Sand grain crushing and interface shearing during displacement pile installation in sand. Géotechnique, **60**(6): 469-482.

Yang, Z. X., Jardine, R. J., Guo, W. B., and Chow, F. 2015a. A new and openly accessible database of tests on piles driven in sands. Géotechnique Letters: **5**(1): 12-20.

Yang, Z. X., Jardine, R. J., Guo, W. B., and Chow, F. 2015b. A comprehensive database of tests on axially loaded piles driven in sand, Zhejiang University Press and Elsevier.

Yang, Z. X., Guo, W. B., Jardine, R. J., and Chow, F. 2017. Design method reliability assessment from an extended database of axial load tests on piles driven in sand. Canadian Geotechnical Journal, **54**(1): 59-74.

Yang, Z. X., Gao, Y. Y., Jardine, R. J., Guo, W. B., and Wang, D. 2020. Large deformation finite element simulation of displacement pile installation experiments in Sand. Journal of Geotechnical and Geoenvironmental Engineering, **146**(6): 04020044.

Zhang, C., Nguyen, G. D., and Einav, I. 2013. The end-bearing capacity of piles penetrating into crushable soils. Géotechnique, **63**(5): 341-354.

Zhang, C., Yang, Z. X., Nguyen, G. D., Jardine, R. J., and Einav, I. 2014. Theoretical breakage mechanics and experimental assessment of stresses surrounding piles penetrating into dense silica sand. Géotechnique Letters, **4**(1): 11-16.

Zhang, W., Zou, J. Q., Zhang, X. W., Yuan, W. H., and Wu, W. 2021. Interpretation of cone penetration test in clay with smooth particle finite element method. Acta Geotechnica, **16**(2021): 2593-2607

Zhu, B. T., Jardine, R. J., and Foray, P. 2009. The use of miniature soil stress measuring cells in laboratory applications involving stress reversals. Soils and Foundations, **49**(5): 675-688.

Table 1. Model parameters of state-dependent Mohr–Coulomb for NE34 sand

Elastic parameters	Critical state parameters	State-dependent parameters
E = 60 MPa	$\varphi_c = 30°$	$n_d = 1.7$
v = 0.3	$e_\Gamma = 0.9$	$n_b = 2.3$
	$\lambda_c = 0.119$	
	$\zeta = 0.23$	

Table 2. Drained triaxial tests on NE34 sand

Test ID	e_0	p'_0 (kPa)
TM1	0.638	200
TM2	0.584	100
TM3	0.573	200
TM4	0.572	400
TM5	0.637	400

Table 3 Sand stiffness varying with σ_{v0} for parametric analysis

σ_{v0} (kPa)	50	150	250	350	450	550
p/p_a	0.31	0.93	1.55	2.17	2.79	3.41
$E_{varible}$ (MPa)	34.6	60.0	77.4	91.6	103.9	114.9

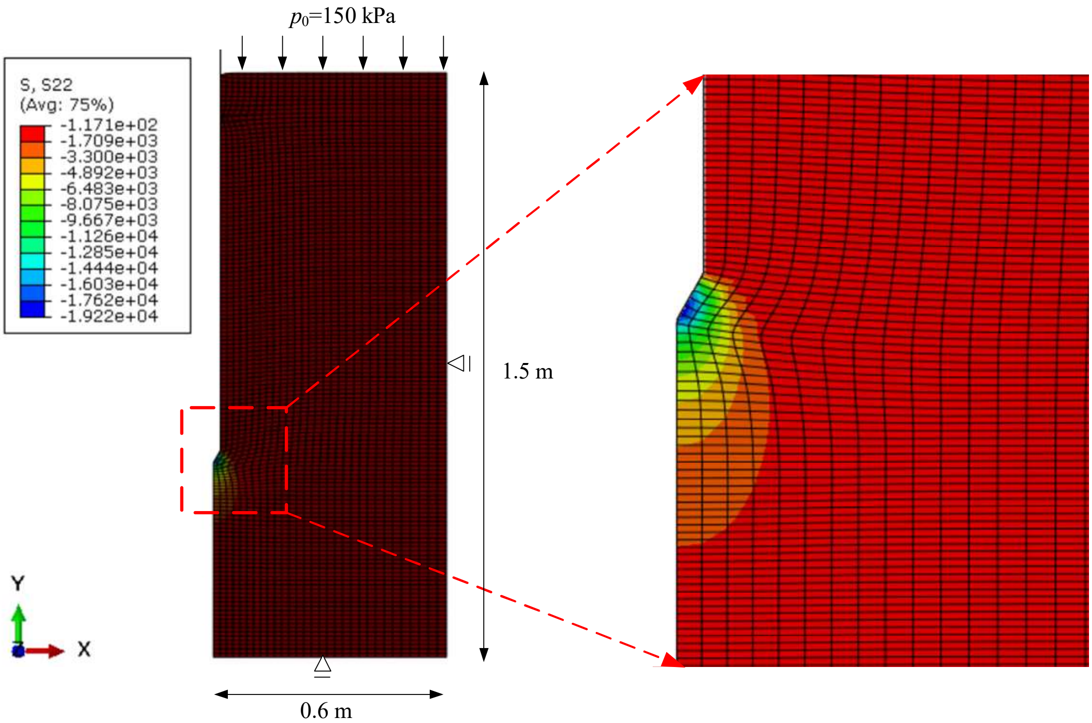

Fig. 1 Numerical model and the vertical stresses contours during the last stroke of penetration

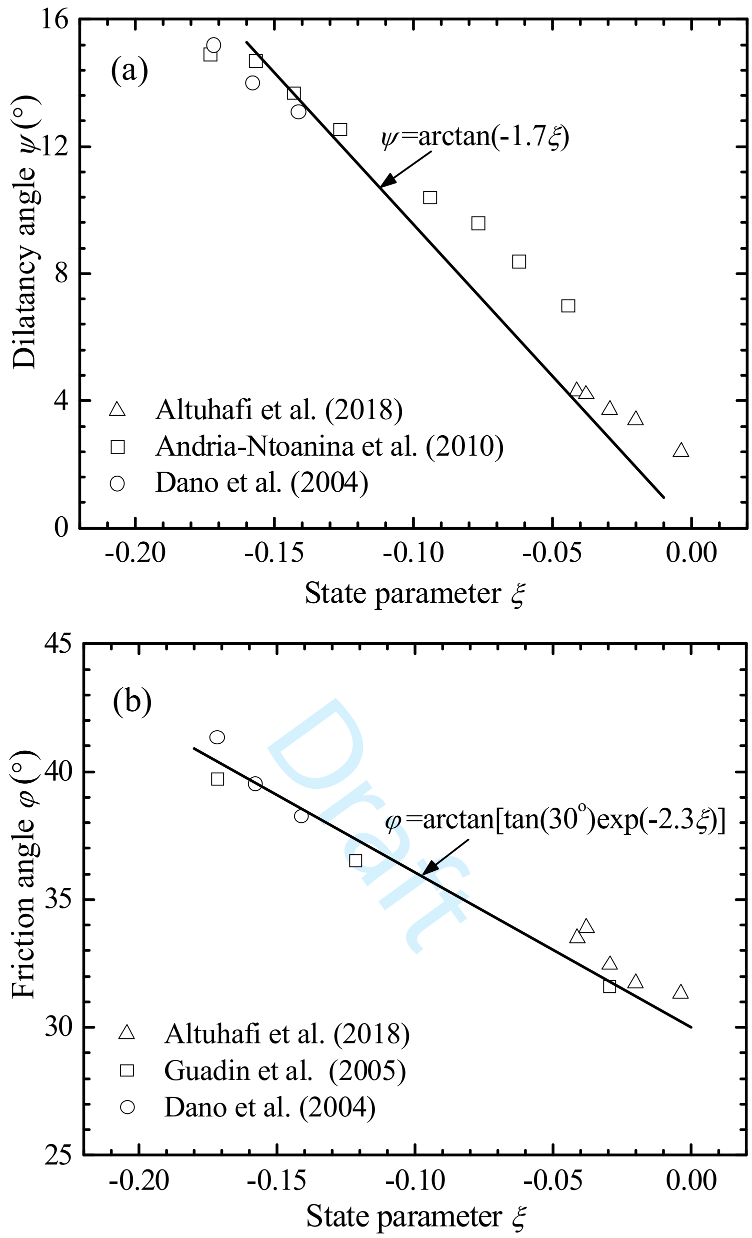

Fig. 2 Relationships between dilatancy angle ψ, friction angle φ and state parameter ξ

(a) dilatancy angle; (b) friction angle

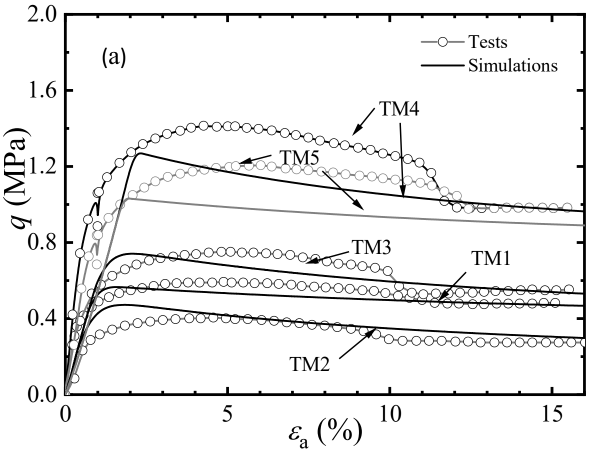

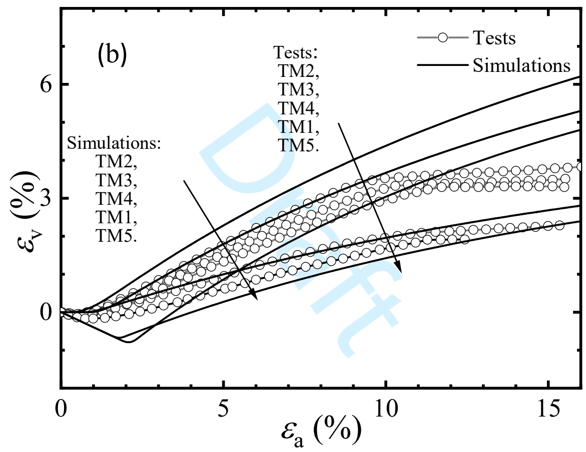

Fig. 3 Comparisons between experimental observations and simulations results of drained triaxial compression tests on Fontainebleau sand

(a) q-ε_a; (b) ε_v-ε_a

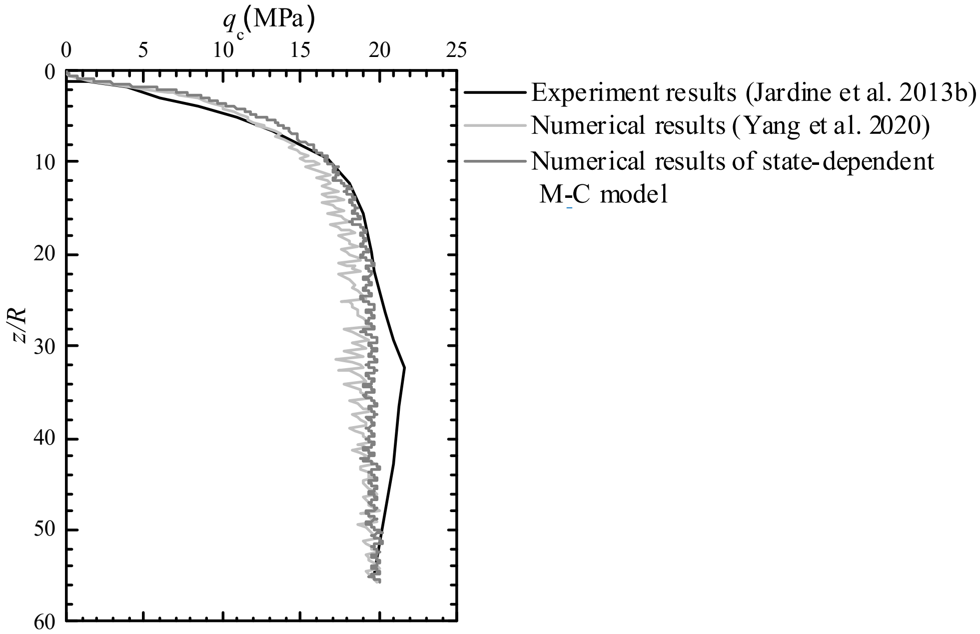

Fig. 4 Comparisons of Calibration Chamber CPT cone resistance q_c profiles

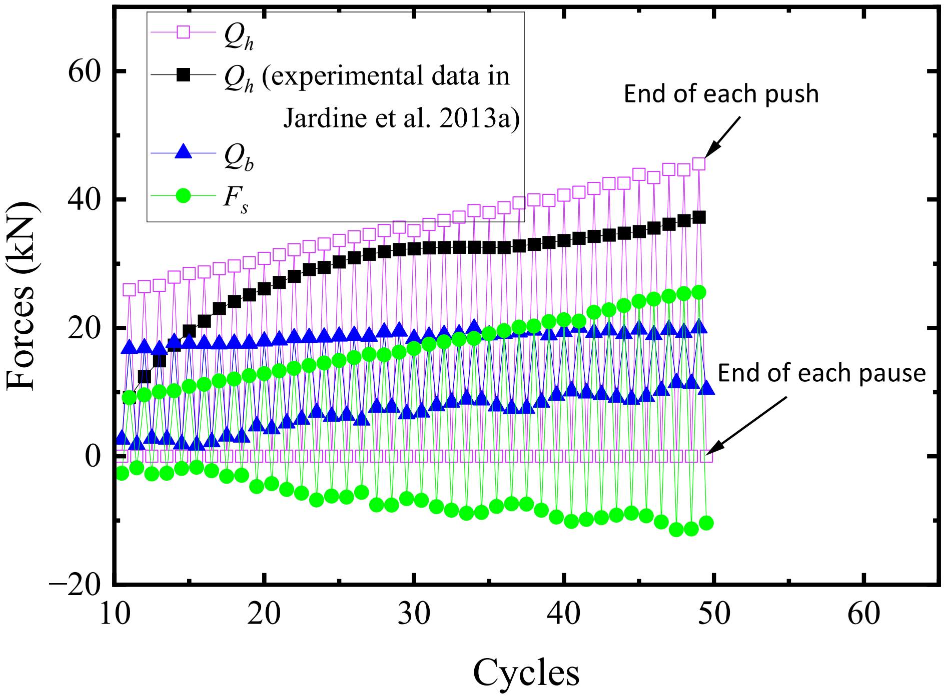

Fig. 5 Development of head/base forces Q_h, Q_b and shaft friction forces F_s.

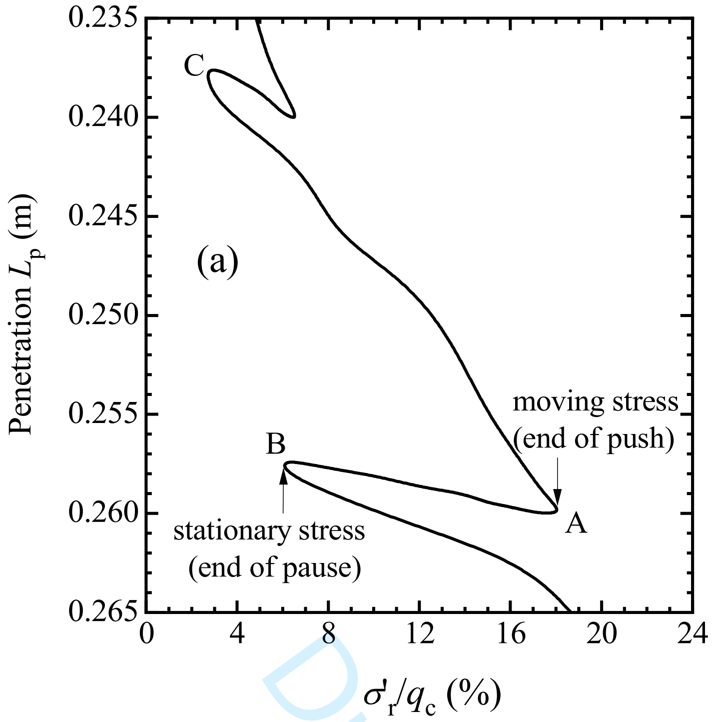

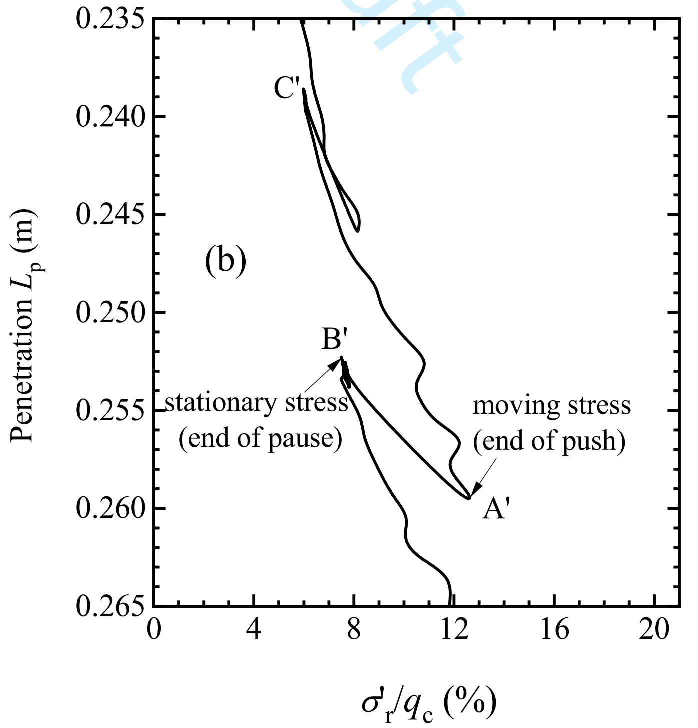

Fig. 6 Illustrations of normalized radial stress profiles (r/R=2) measured in the sand mass during penetration

(a) experimental data (Rimoy 2013); (b) numerical results

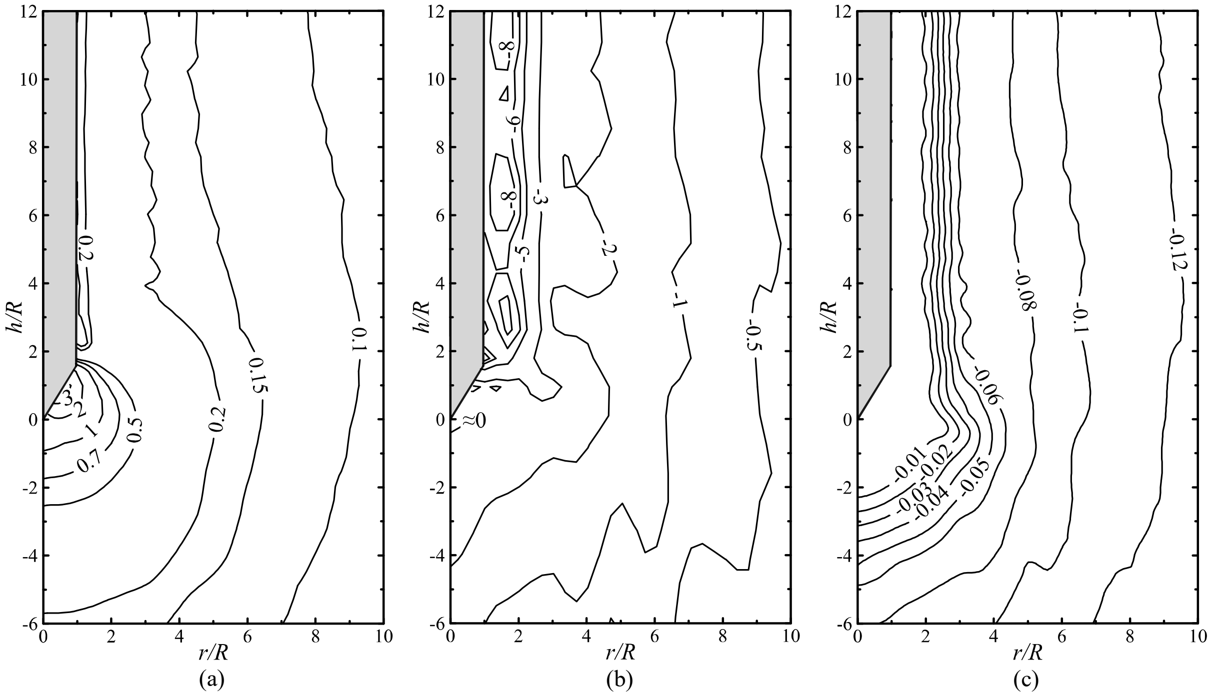

Fig. 7 Sand state contours adjacent to the pile after penetration in terms of
(a) mean normal stress (MPa); (b) volumetric strain (%); (c) state parameter of sand mass

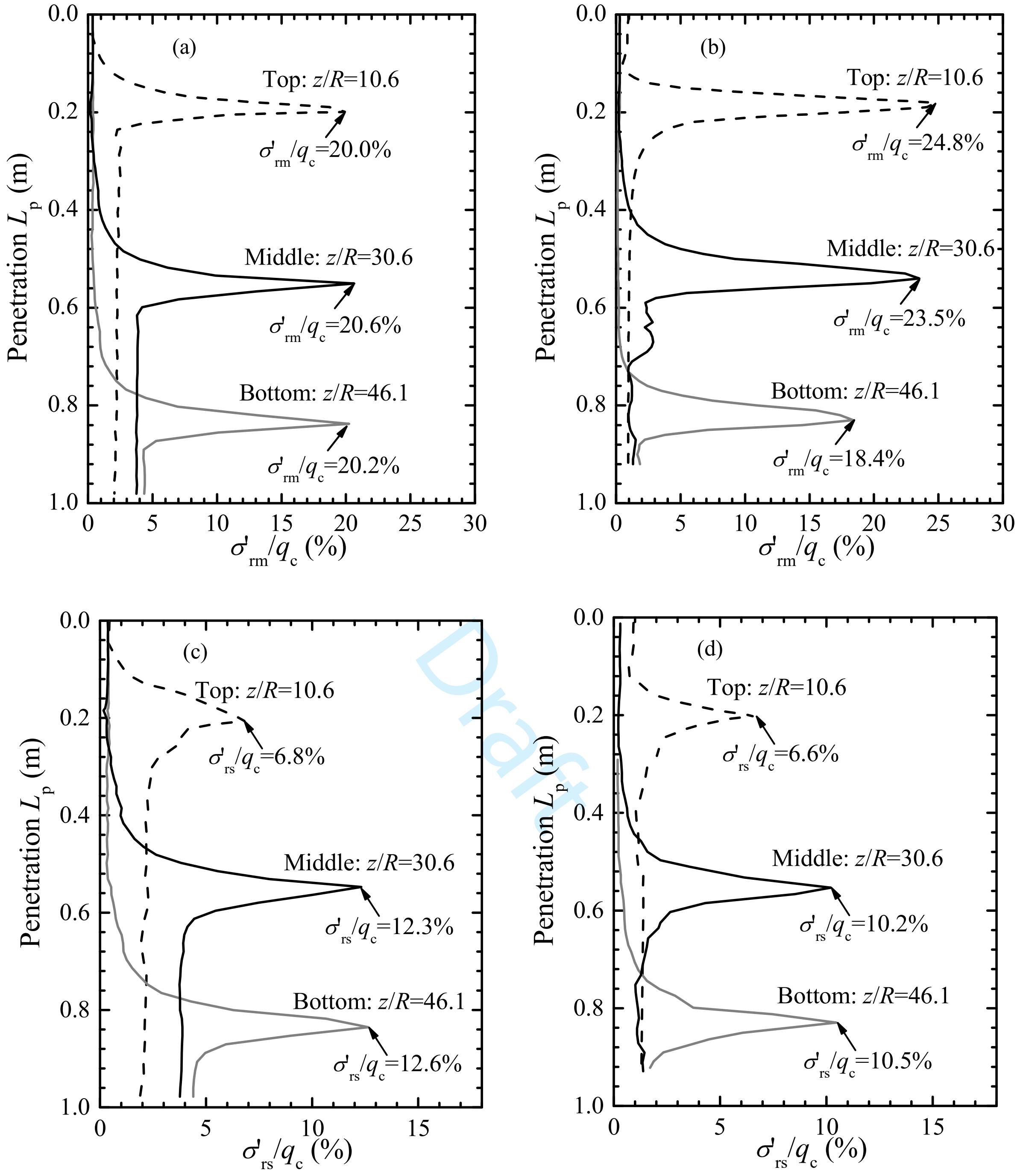

Fig. 8 Normalized radial stresses measured at r/R = 2 during penetration

(a) numerical results (moving); (b) experimental results (moving); (c) numerical results (stationary); (d) experimental results (stationary)

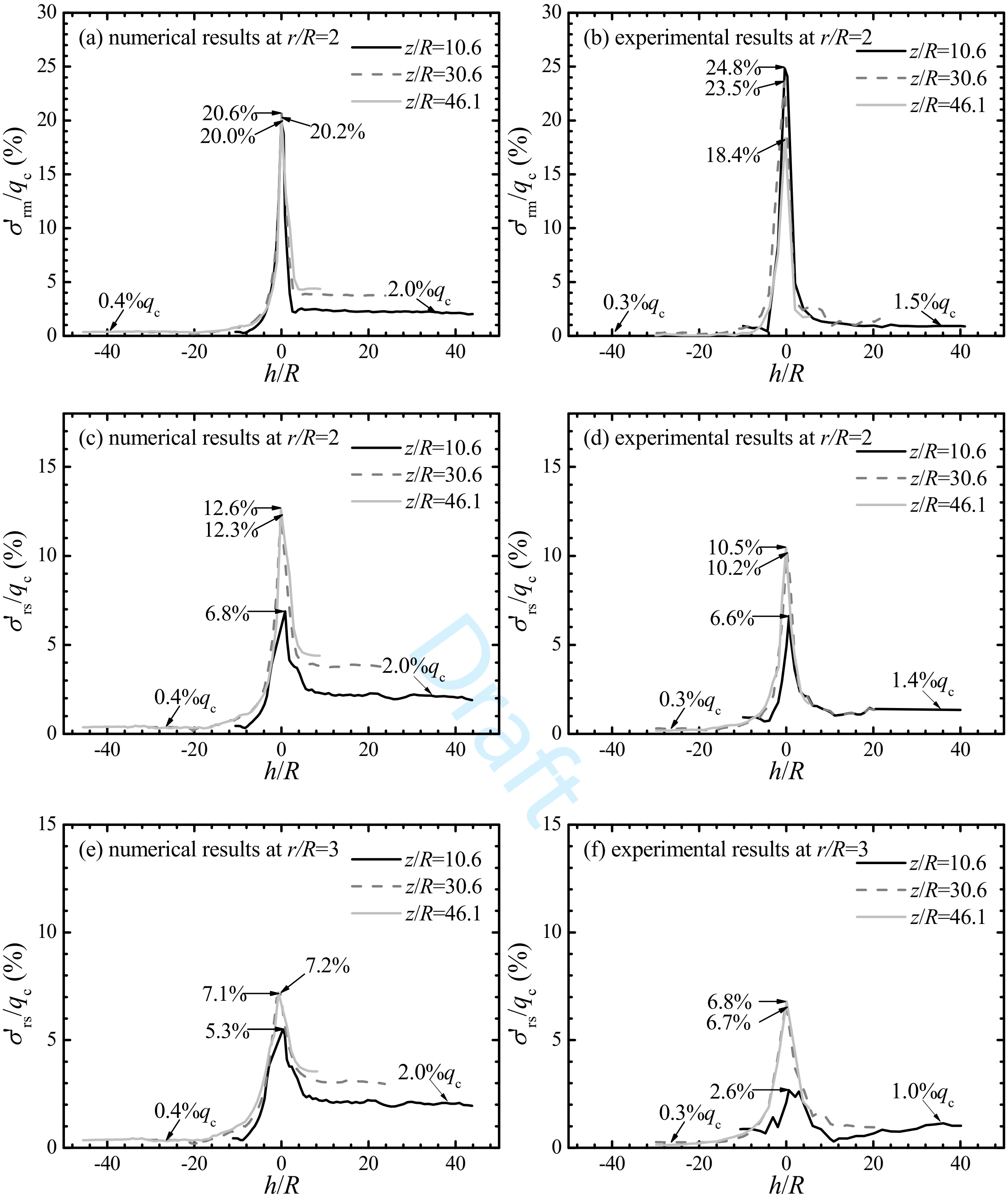

Fig. 9 Normalized radial stresses plotted against relative pile tip depth *h*/*R* measured at *r*/*R* = 2

(a) 'moving' (numerical); (b) 'moving' (experimental);

(c) 'stationary' (numerical); (d) 'stationary' (experimental)

and *r*/*R* = 3

(e) 'stationary' (numerical); (f) 'stationary' (experimental)

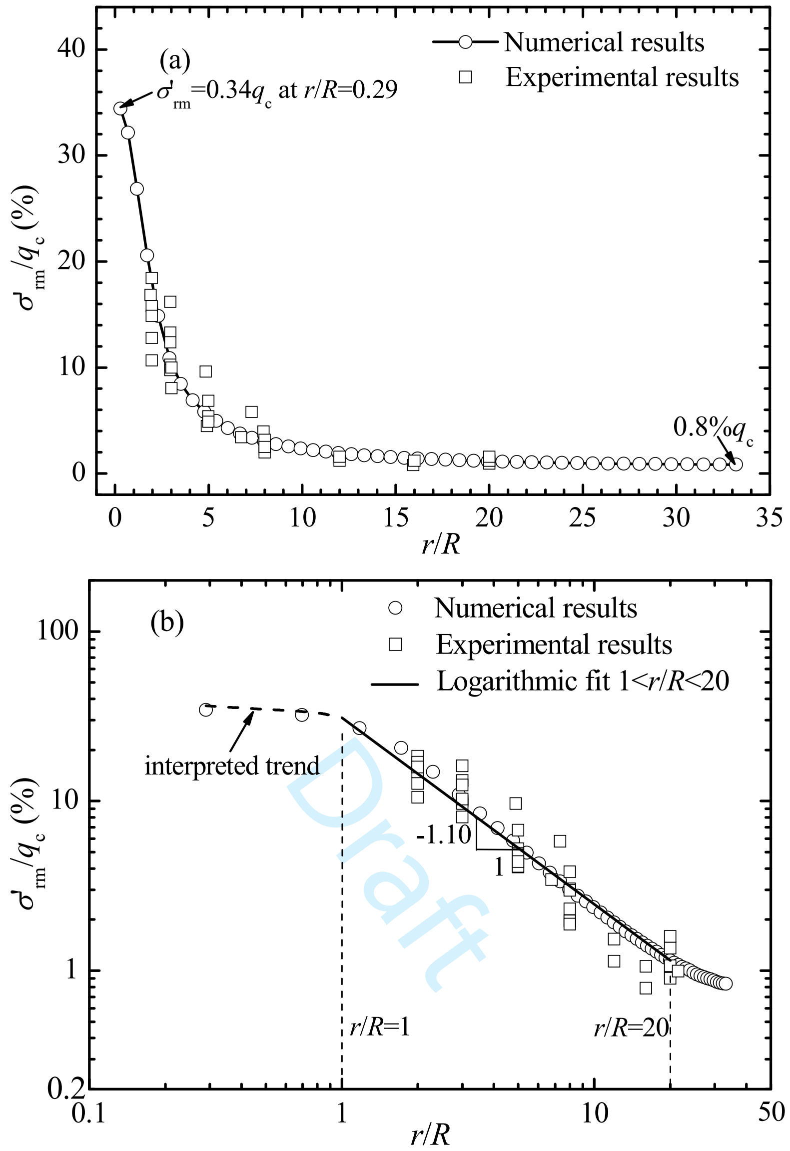

Fig. 10 Non-dimensional moving radial stresses developed at *h/R* = 0.5 during penetration

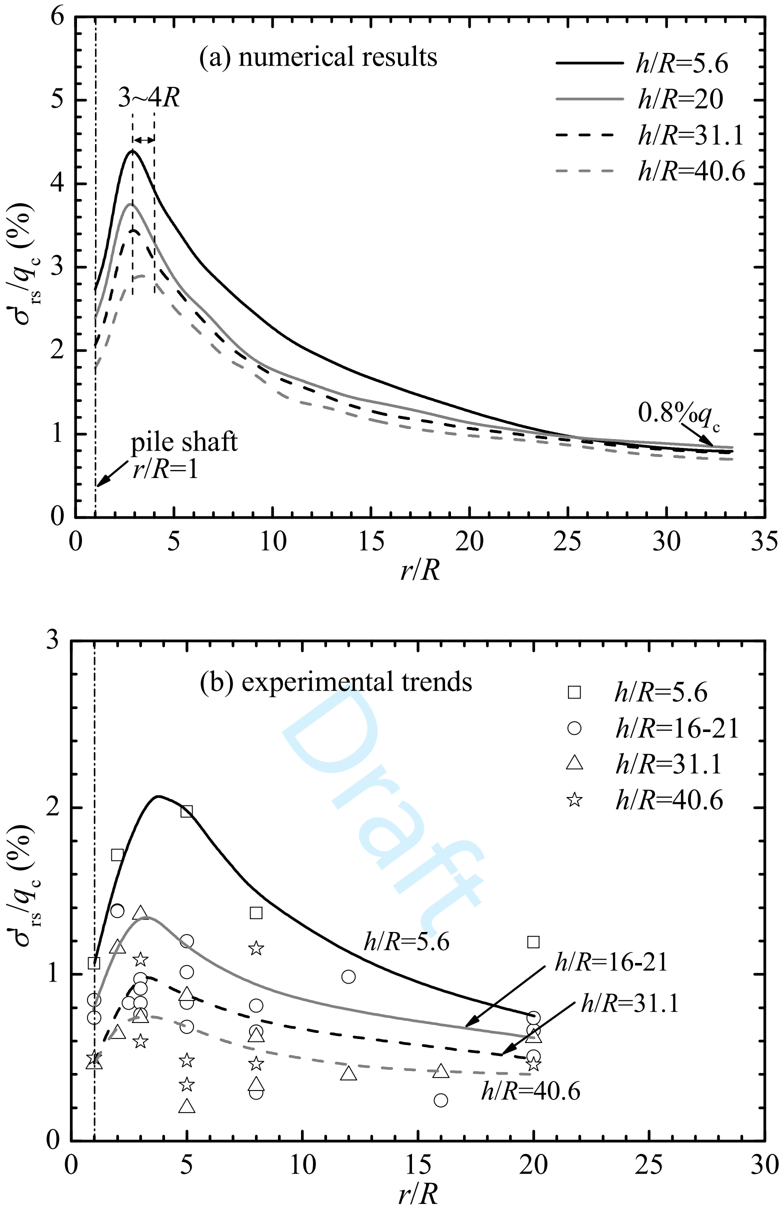

Fig. 11 Radial stresses acting above tip (*h/R* >5) at the end of penetration
(a) numerical results; (b) experimental trends

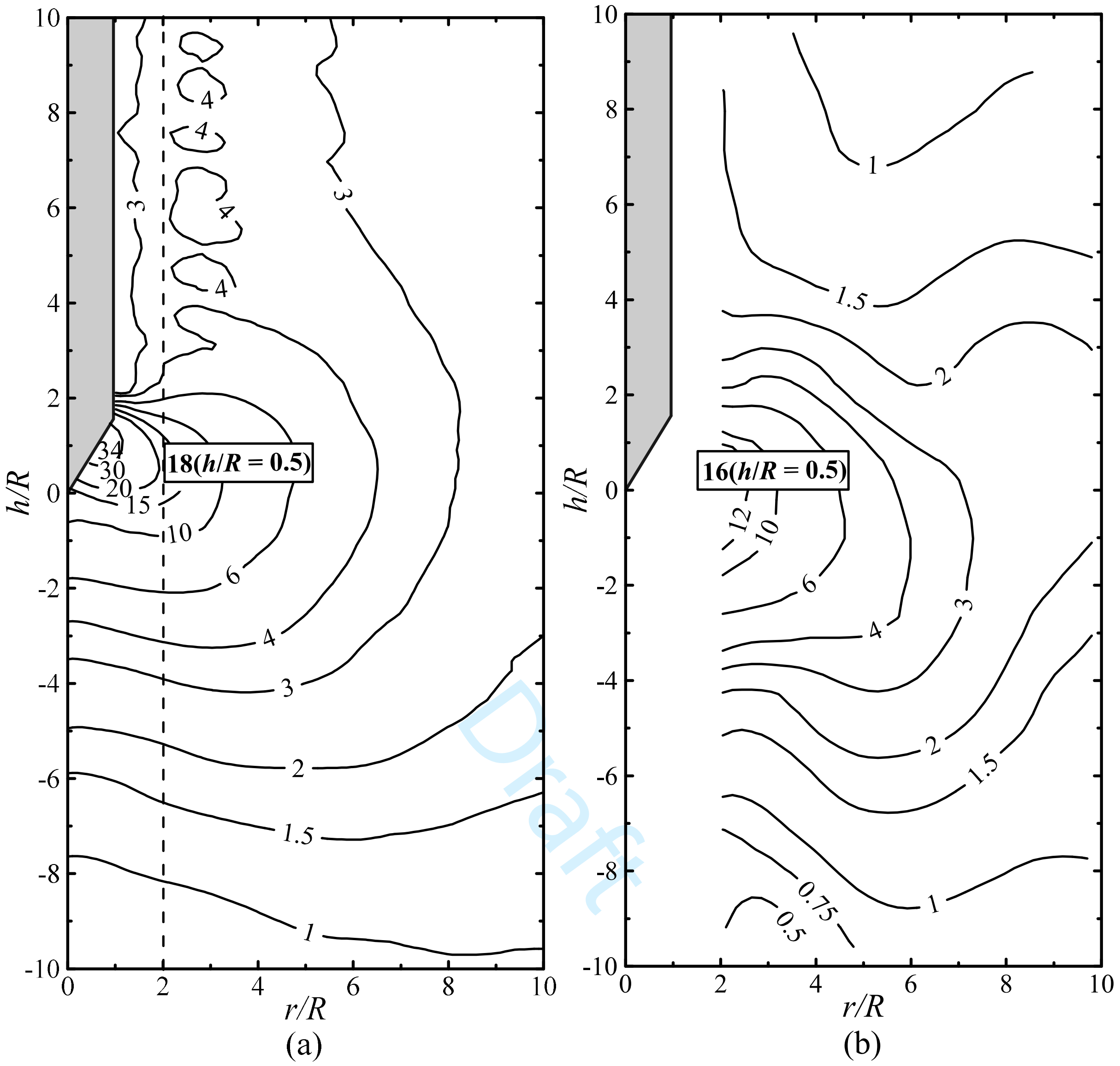
18(h/R = 0.5)
16(h/R = 0.5)
h/R
r/R
(a)
(b)
34
30
20
15
10
6
4
3
2
1.5
1
12
0.75
0.5
Draft

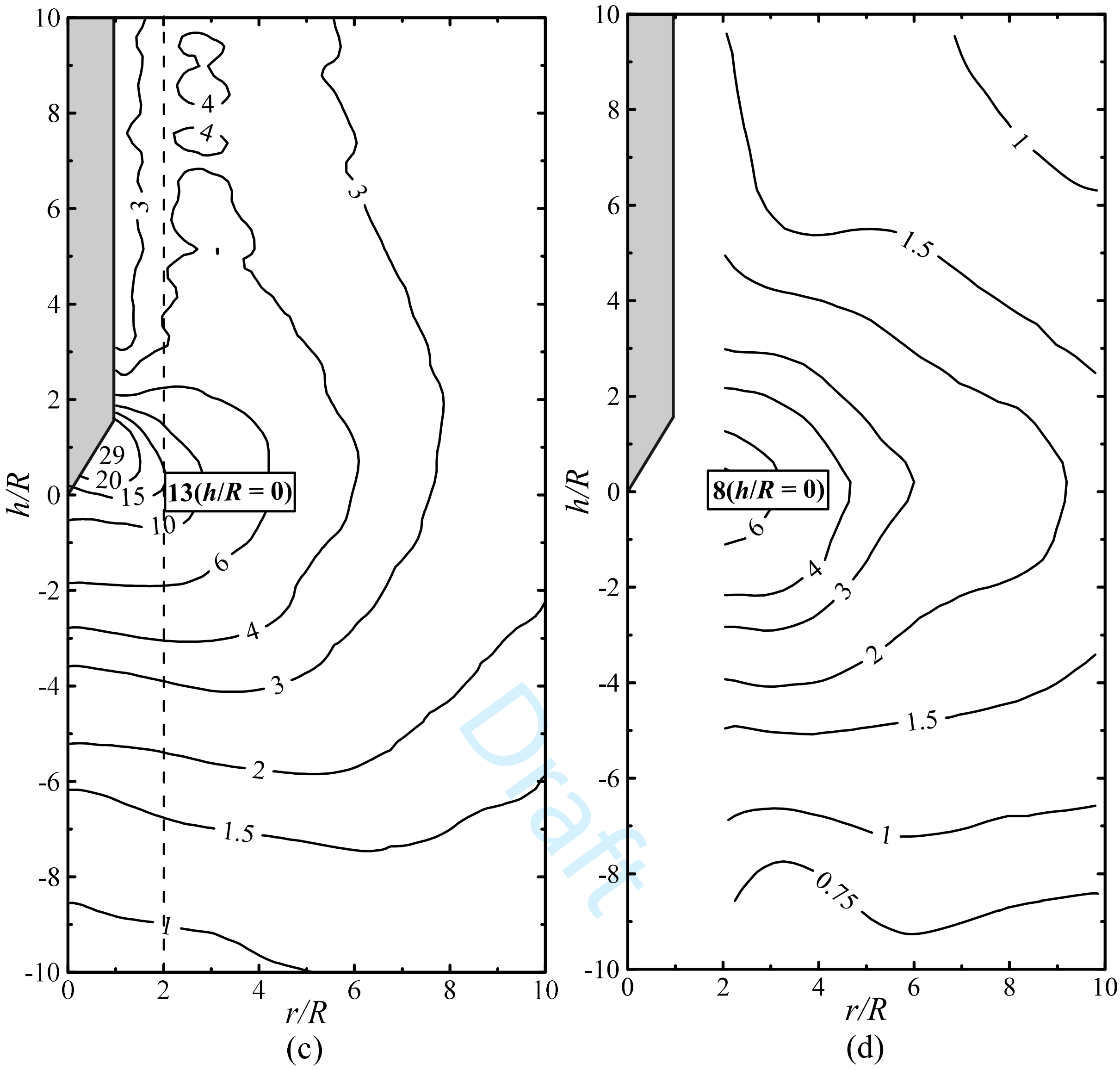

Fig. 12 Normalized radial stress contours adjacent to pile tip during the last stroke of penetration
(a) 'moving' (numerical); (b) 'moving' (experimental);
(c) 'stationary' (numerical); (d) 'stationary' (experimental)

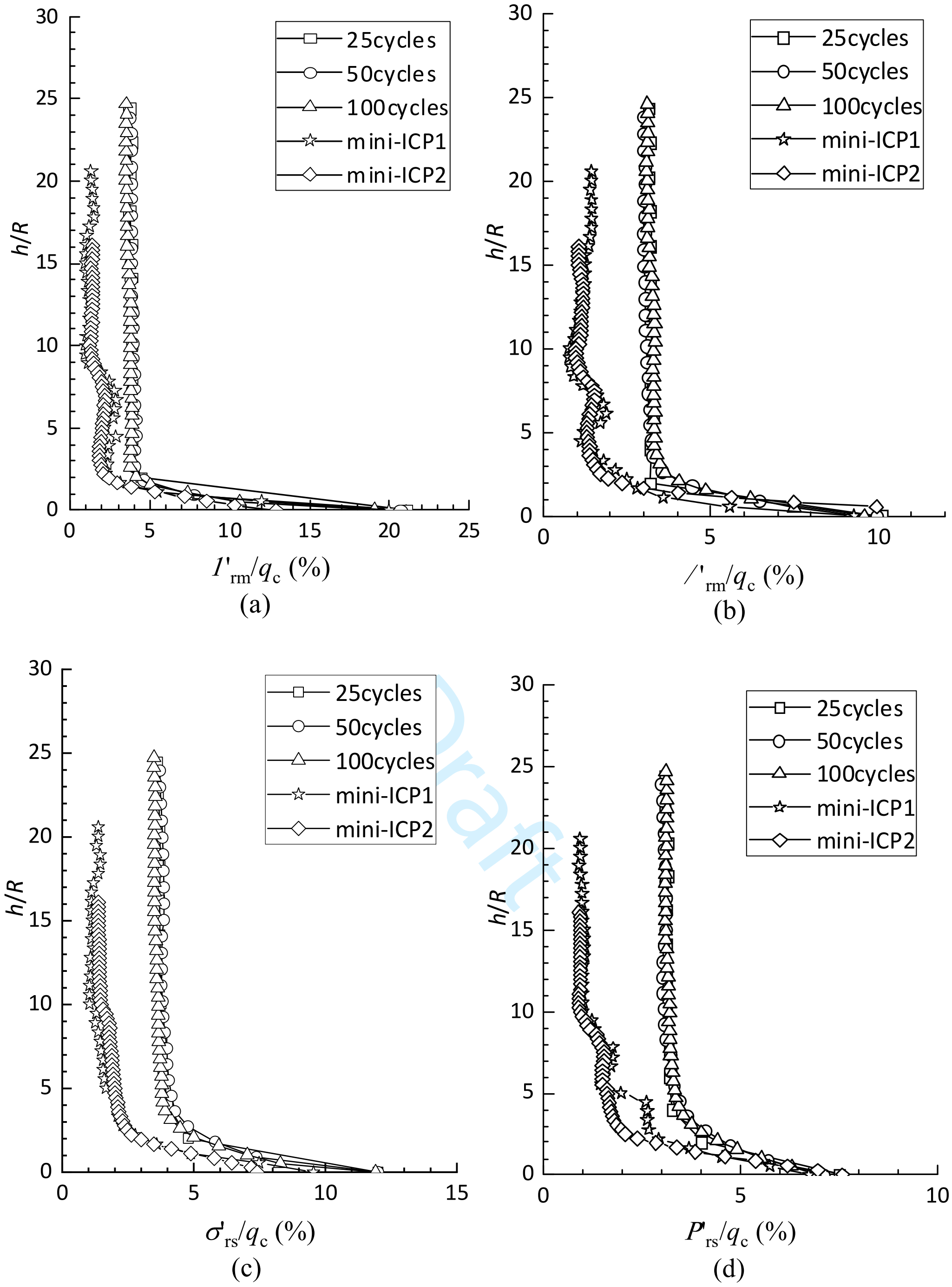
25cycles
50cycles
100cycles
mini-ICP1
mini-ICP2
h/R
(a)
(b)
σ'rs/qc (%)
(c)
P'rs/qc (%)
(d)

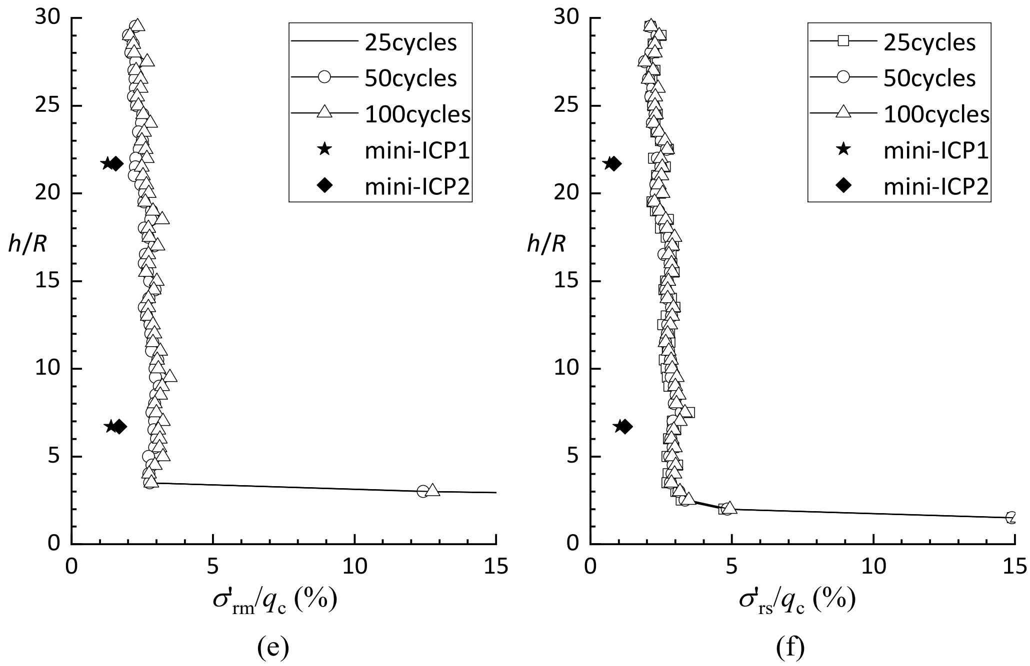

Fig. 13 Influences of h/R on the moving radial stresses at (a) r=2R, (b) r=3R and (e) r=R, and stationary radial stresses at (c) r=2R, (d) r=3R and (f) r=R

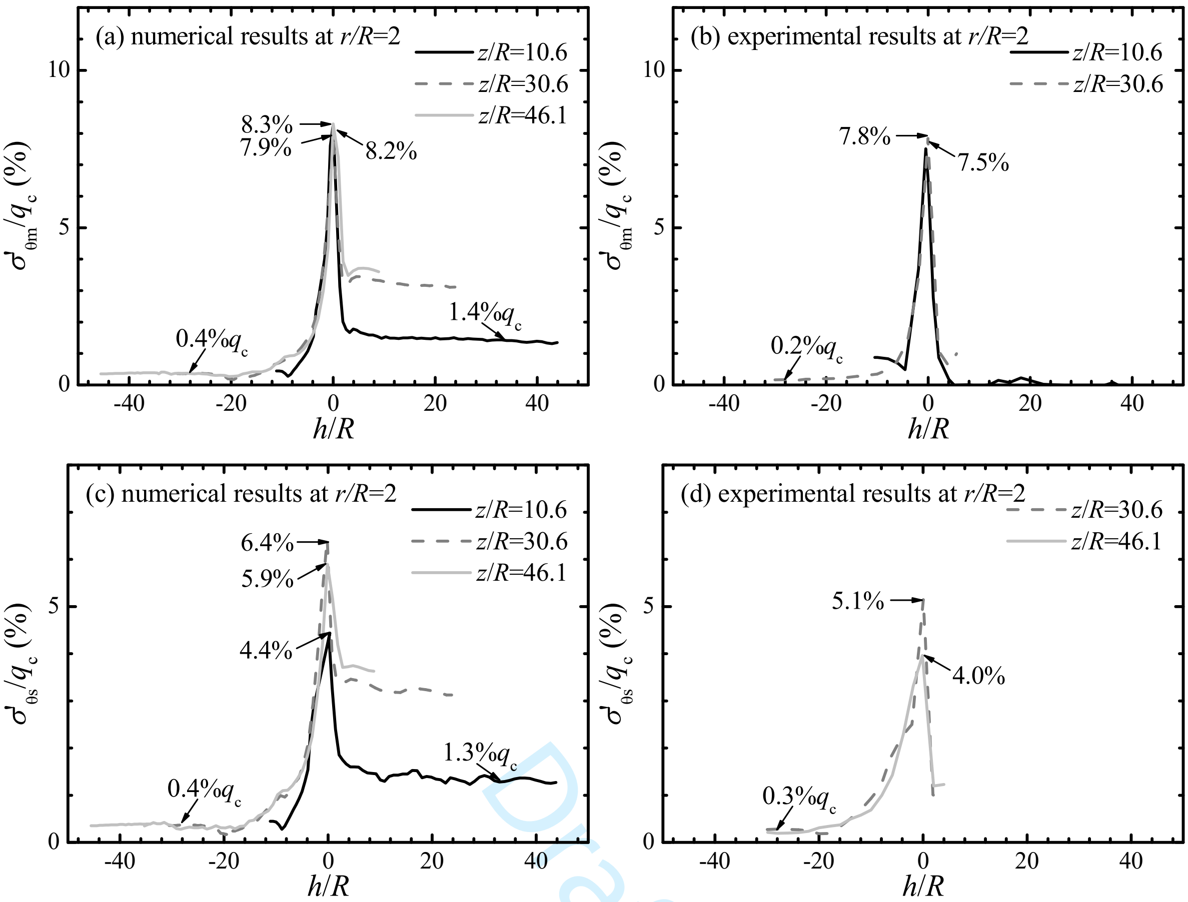

Fig. 14 Normalized circumferential stresses plotted against relative pile tip depth h/R measured at r/R = 2

(a) 'moving' (numerical); (b) 'moving' (experimental);

(c) 'stationary' (numerical); (d) 'stationary' (experimental)

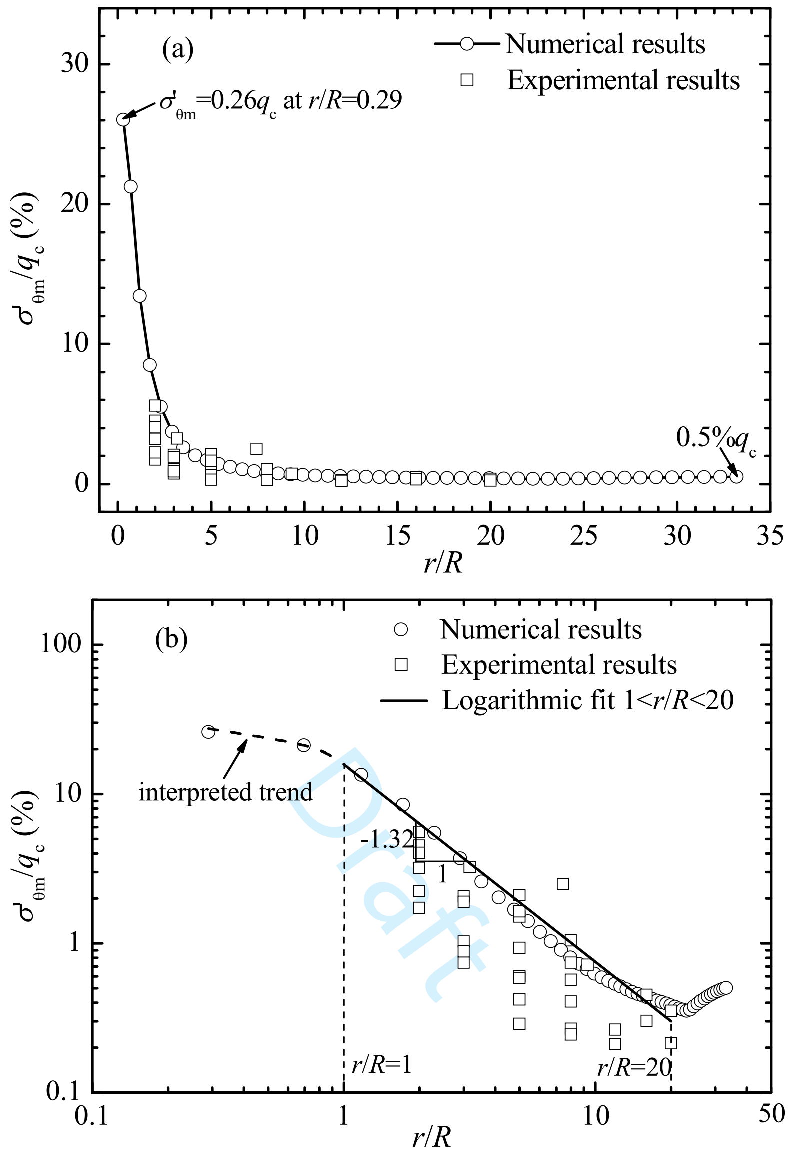

Fig. 15 Non-dimensional moving circumferential stresses developed at h/R = 0.5 during penetration

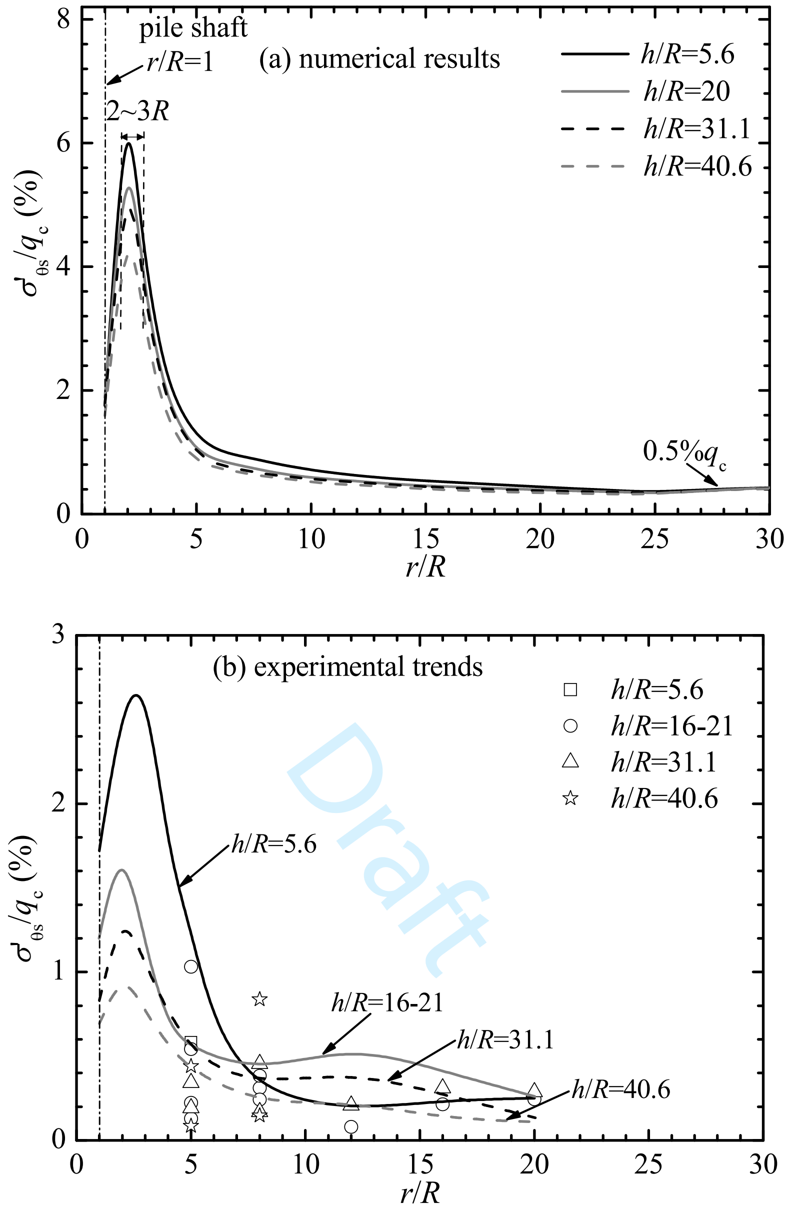

Fig. 16 Circumferential stresses acting above tip (h/R >5) at the end of penetration
(a) numerical results; (b) experimental trends

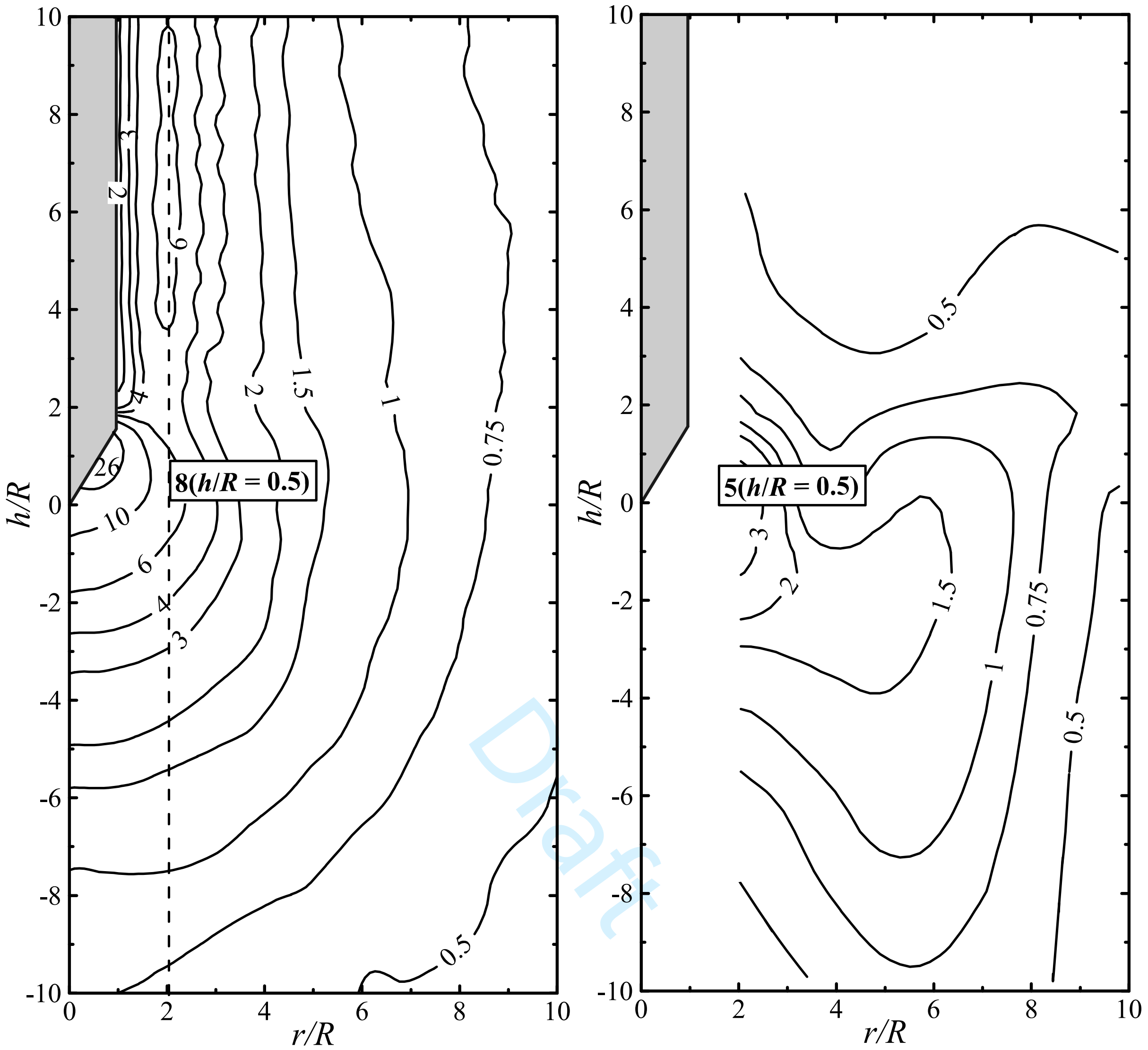

(a) (b)

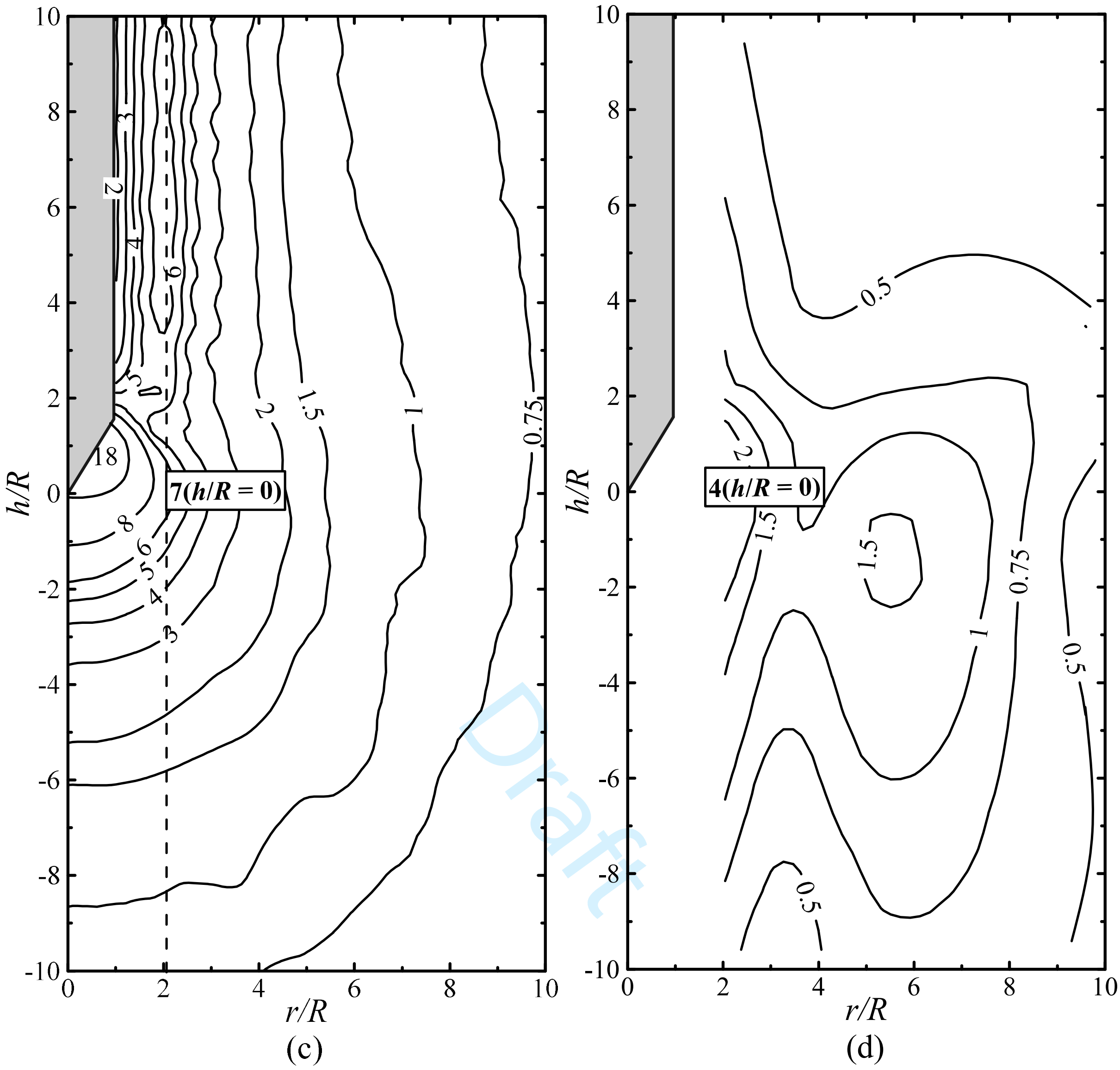

Fig. 17 Normalized circumferential stress contours adjacent to pile tip during the last stroke of penetration (a) 'moving' (numerical); (b) 'moving' (experimental); (c) 'stationary' (numerical); (d) 'stationary' (experimental)

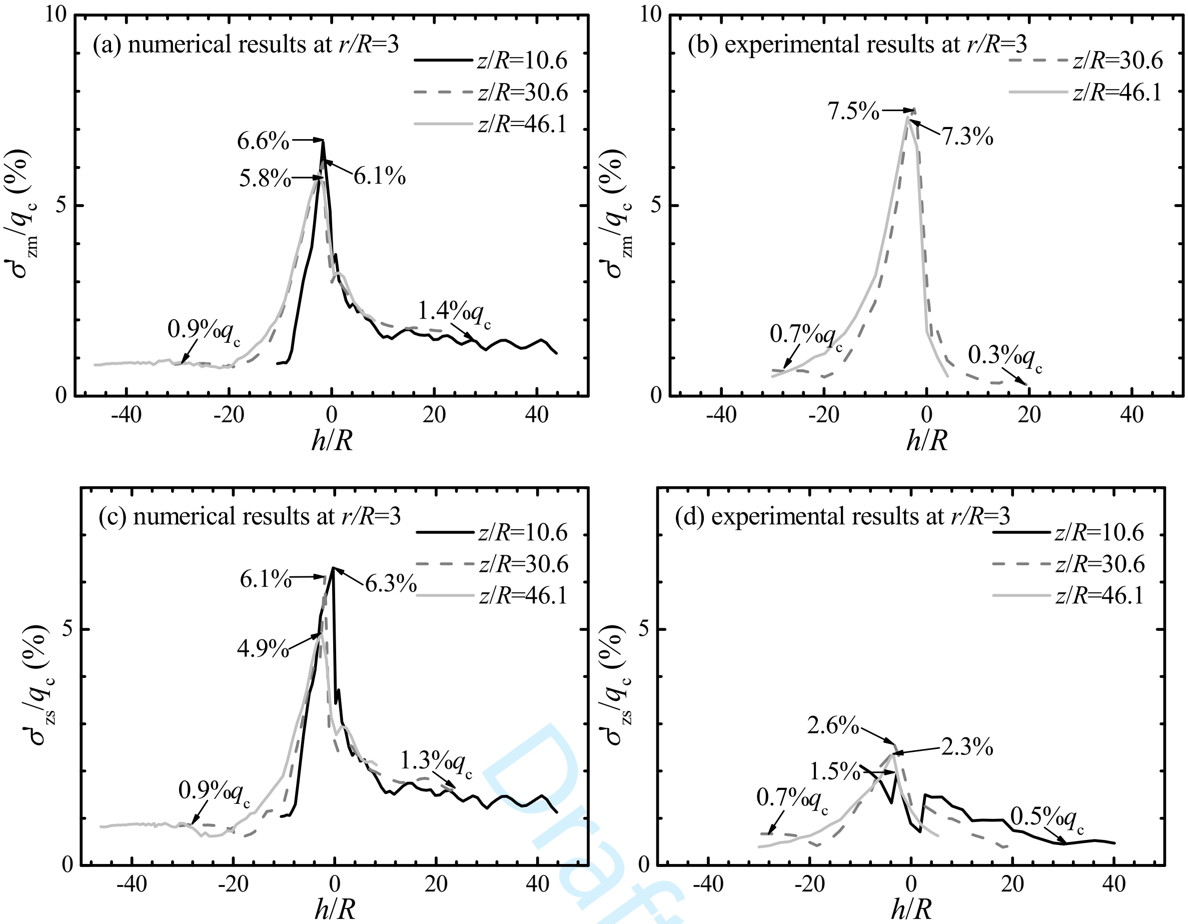

Fig. 18 Normalized vertical stresses plotted against relative pile tip depth *h/R* measured at *r/R* = 3
(a) 'moving' (numerical); (b) 'moving' (experimental);
(c) 'stationary' (numerical); (d) 'stationary' (experimental)

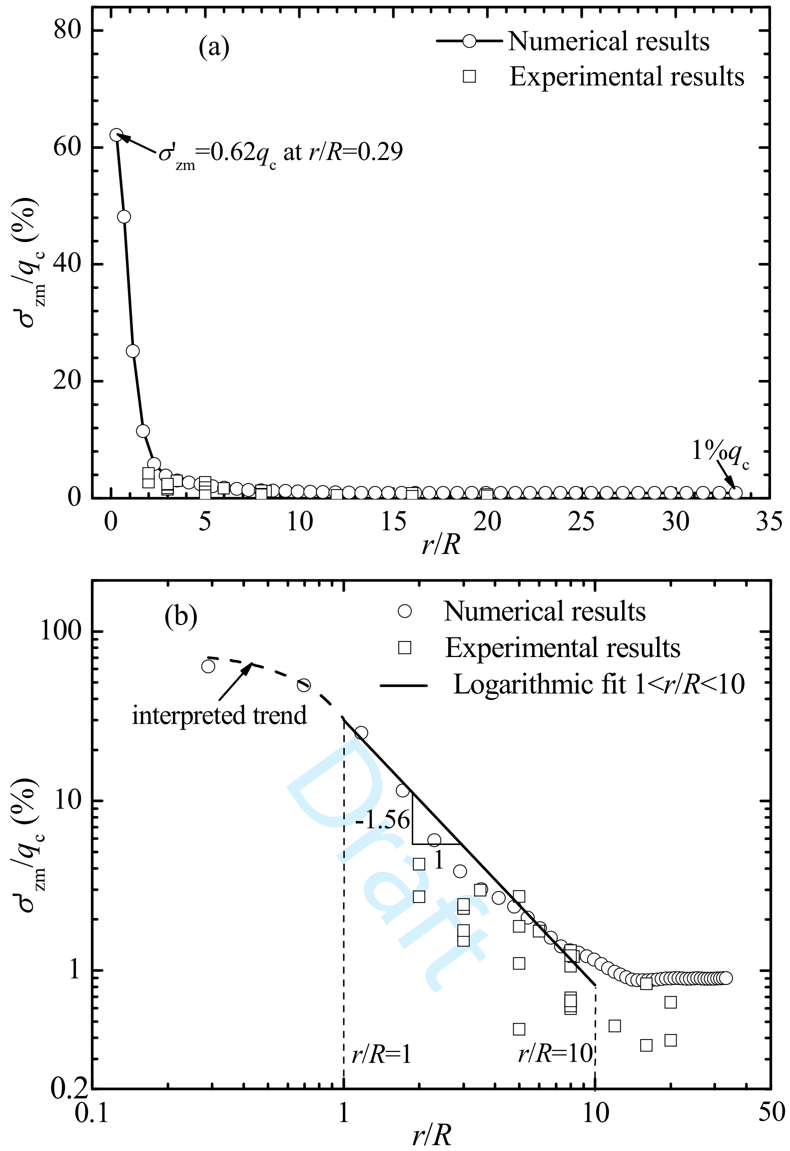

Fig. 19 Non-dimensional vertical stresses developed at h/R=0.5 during penetration

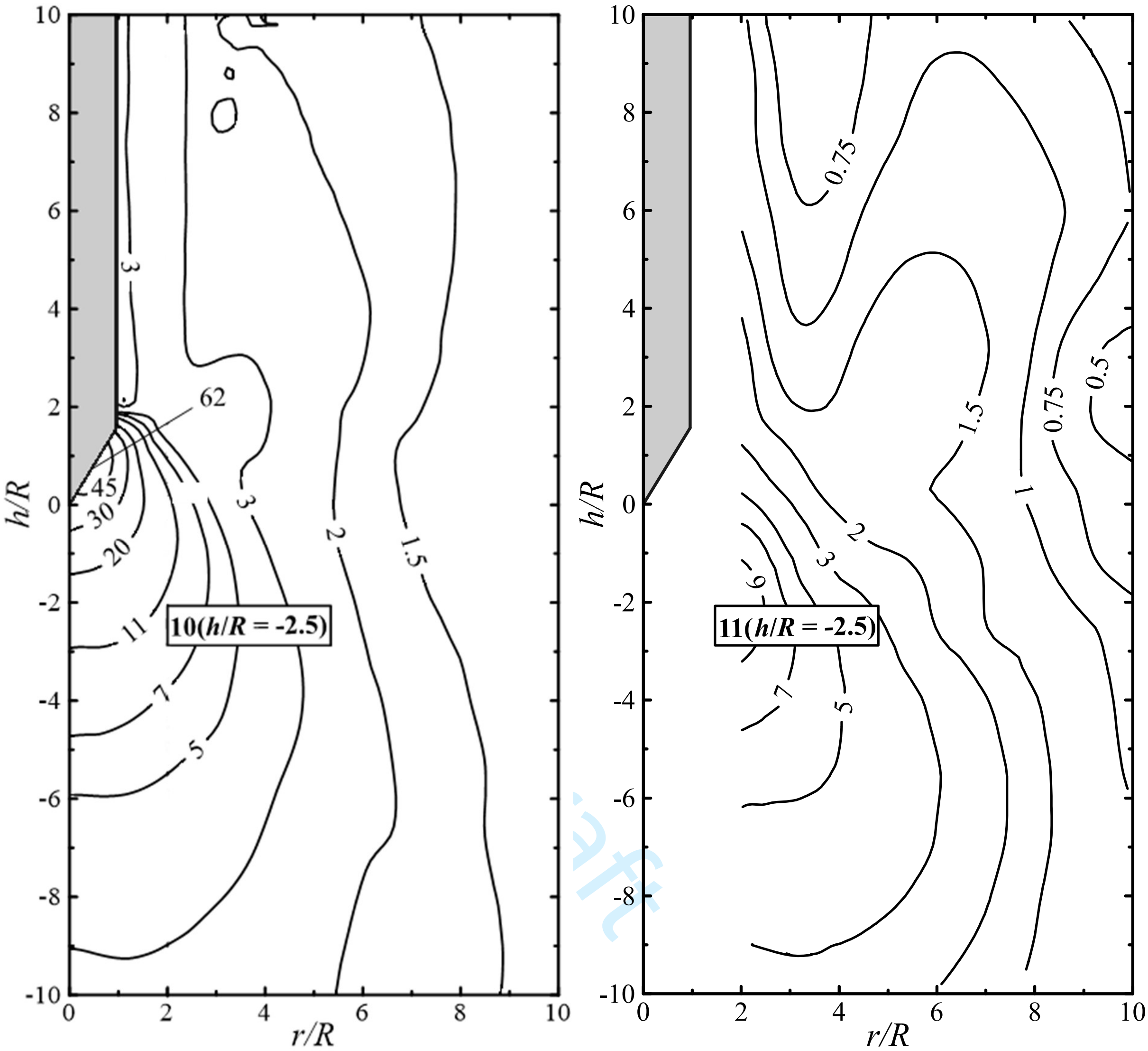
10
8
6
4
2
0
-2
-4
-6
-8
-10
h/R
r/R
3
62
45
30
20
11
7
5
3
2
1.5
10(h/R = -2.5)
0.75
1.5
1
0.75
0.5
2
3
9
7
5
11(h/R = -2.5)

(a) (b)

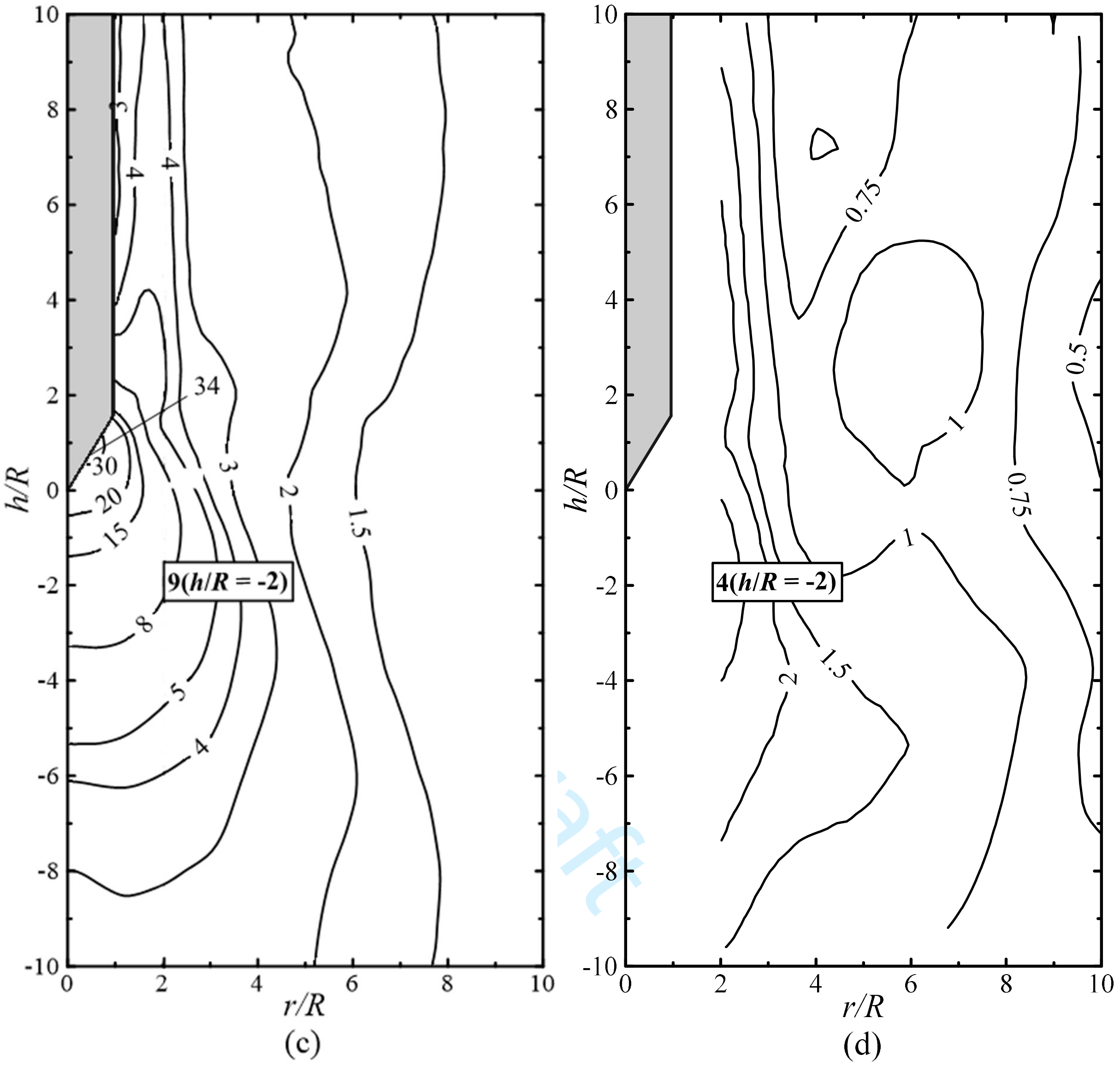

Fig. 20 Normalized vertical stress contours adjacent to pile tip during the last stroke of penetration
(a) 'moving' (numerical); (b) 'moving' (experimental);
(c) 'stationary' (numerical); (d) 'stationary' (experimental)

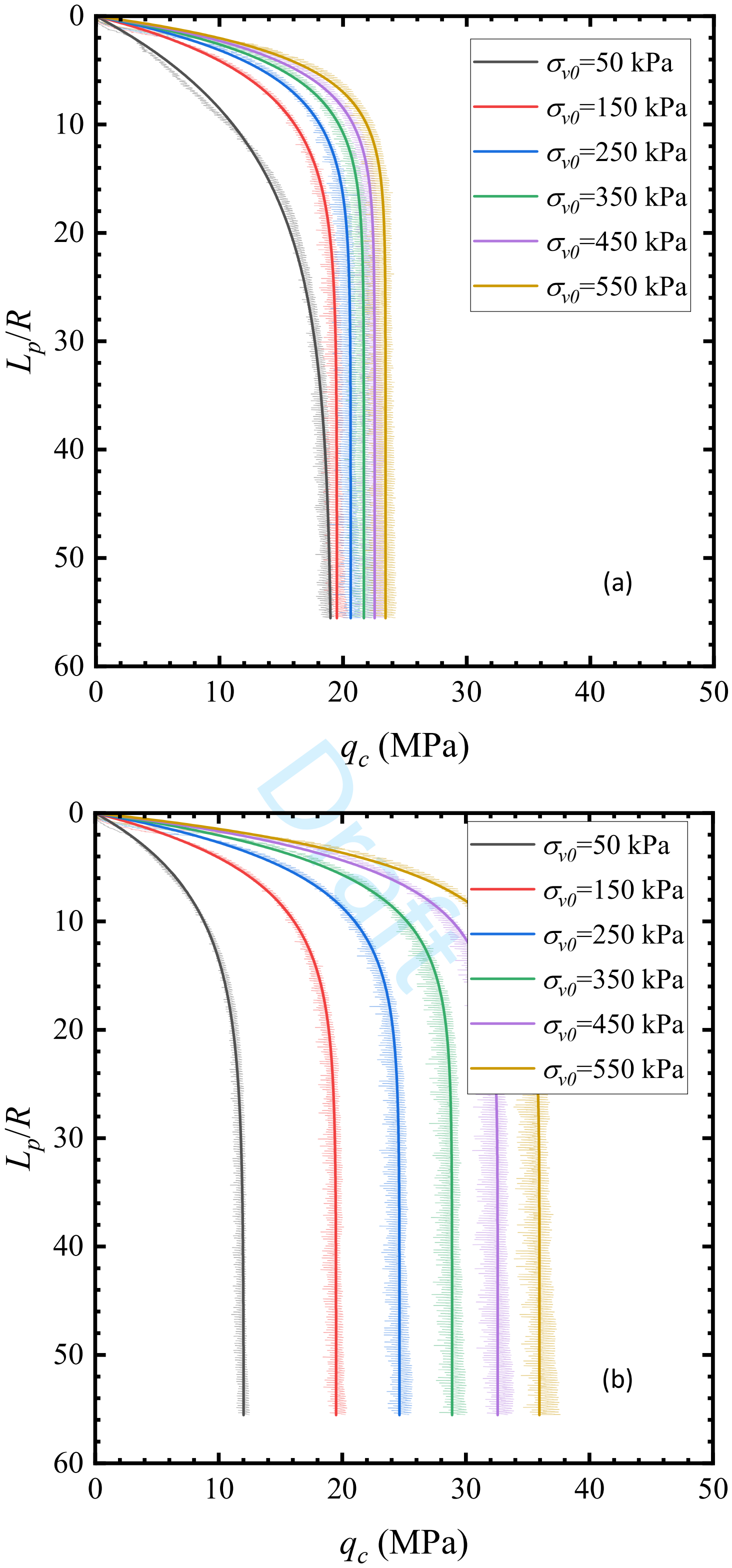

Fig. 21 cone resistance q_c profiles :(a) fixed modulus model, and (b) variable modulus model

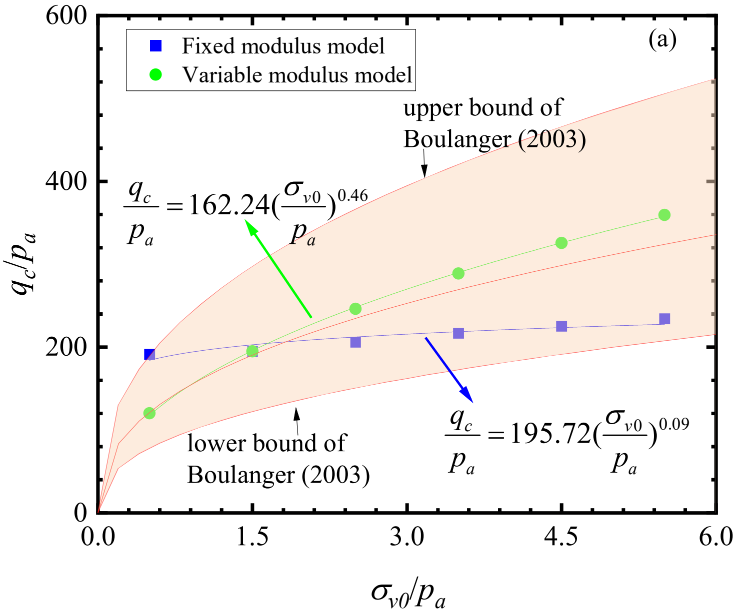

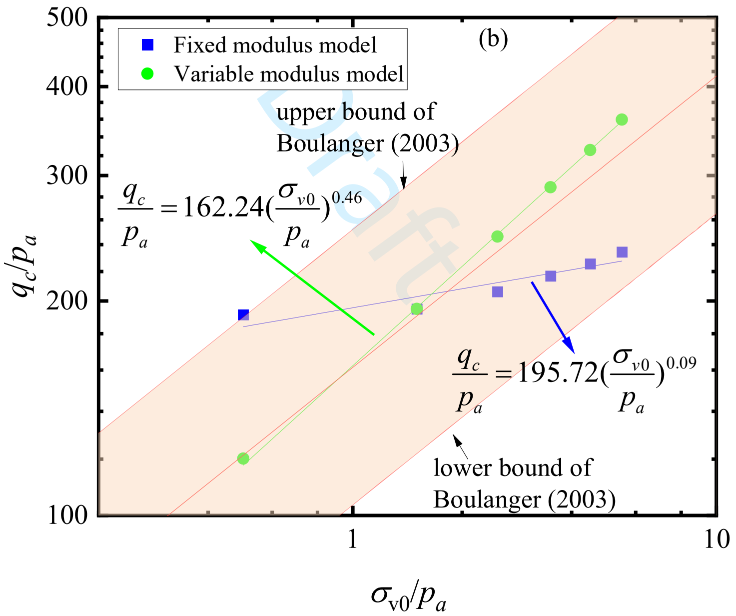

Fig. 22 Comparison of the stable q_c given by simulations and empirical formula: (a) linear scale, (b) log-log scale

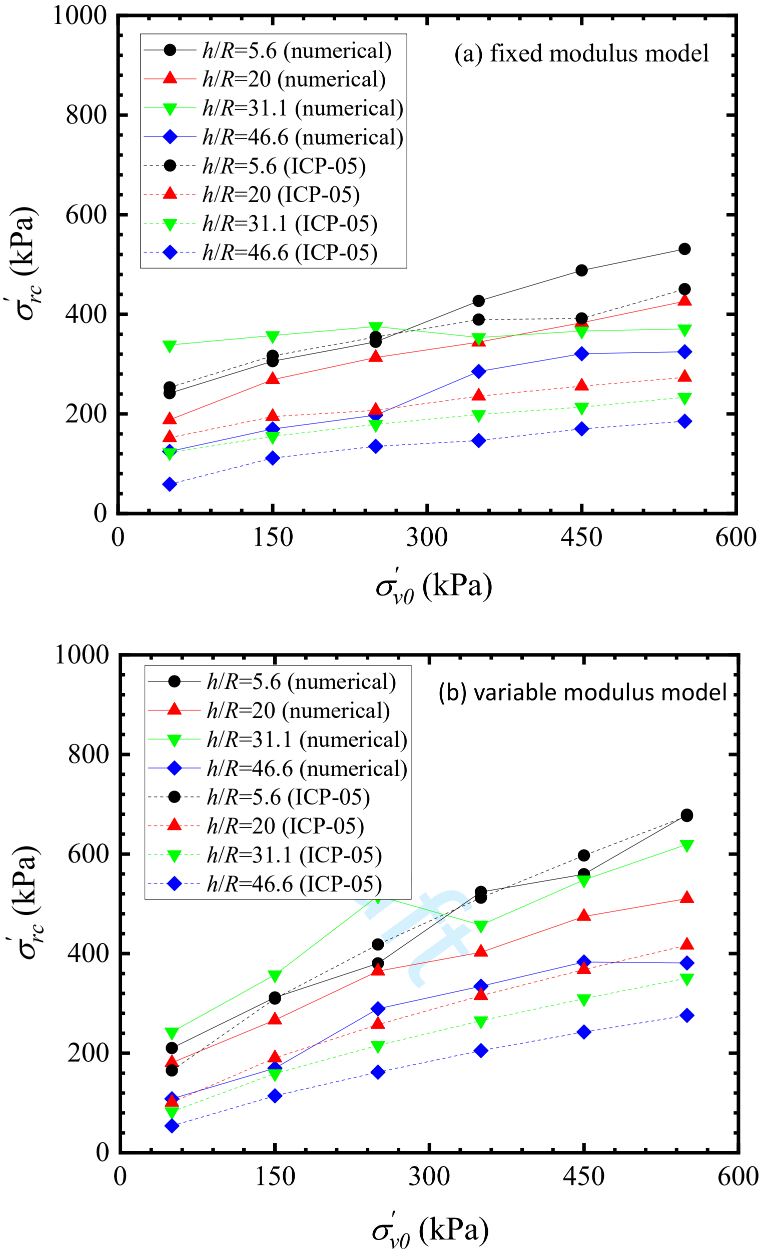

Fig. 23 Comparison of the radial stresses on pile shaft at different height levels predicted by simulations with ICP predictions: (a)fixed modulus model, (b) variable modulus model

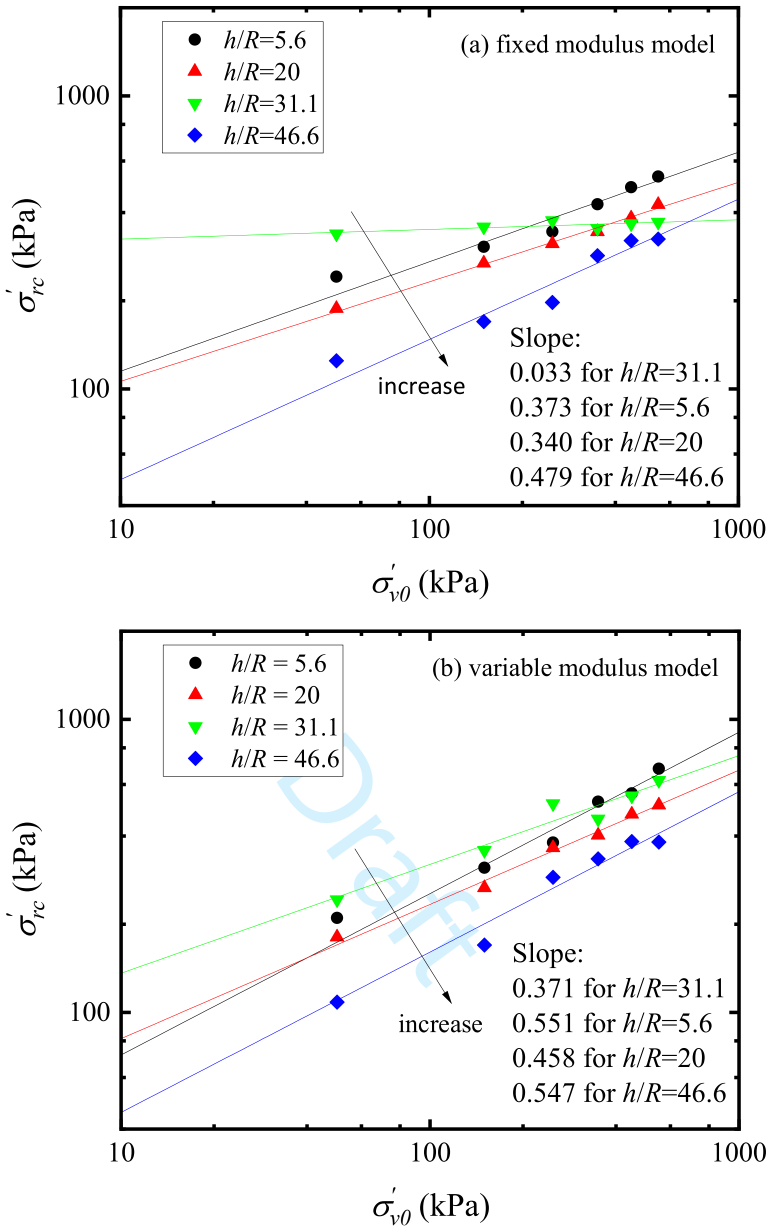

Fig. 24 Influences of σ'_{v0} on σ'_{rc} and their log-log function fitting: (a) fixed modulus model, (b) variable modulus model

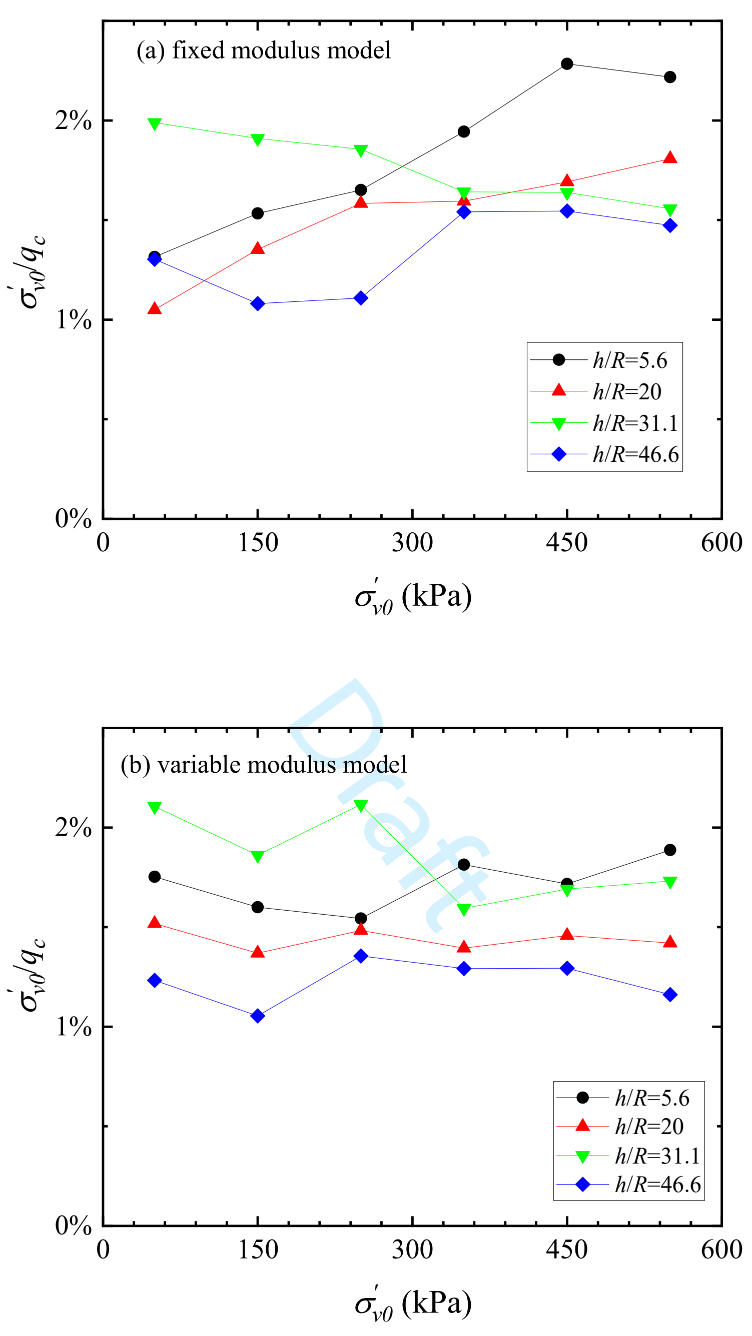

Fig. 25 Influences of σ'$_{v0}$ on the σ'$_{rc}$/q_c ratios at different height levels:
(a) fixed modulus model, (b) variable modulus model